

High-transconductance stretchable transistors achieved by controlled gold microcrack morphology

Matsuhisa, Naoji; Jiang, Ying; Liu, Zhiyuan; Chen, Geng; Wan, Changjin; Kim, Yeongin; Kang, Jiheong; Tran, Helen; Wu, Hung-Chin; You, Insang; Bao, Zhenan; Chen, Xiaodong

2019

Matsuhisa, N., Jiang, Y., Liu, Z., Chen, G., Wan, C., Kim, Y., . . . Chen, X. (2019).
High-transconductance stretchable transistors achieved by controlled gold microcrack
morphology. *Advanced Electronic Materials*, 5(8), 1900347-. doi:10.1002/aelm.201900347

<https://hdl.handle.net/10356/137859>

<https://doi.org/10.1002/aelm.201900347>

This is the peer reviewed version of the following article: Matsuhisa, N., Jiang, Y., Liu, Z., Chen, G., Wan, C., Kim, Y., . . . Chen, X. (2019). High-transconductance stretchable transistors achieved by controlled gold microcrack morphology. *Advanced Electronic Materials*, 5(8), 1900347-. doi:10.1002/aelm.201900347, which has been published in final form at <https://doi.org/10.1002/aelm.201900347>. This article may be used for non-commercial purposes in accordance with Wiley Terms and Conditions for Use of Self-Archived Versions.

High-transconductance stretchable transistors achieved by controlled gold microcrack morphology

Naoji Matsuhisa, Ying Jiang, Zhiyuan Liu, Geng Chen, Changjin Wan, Yeongin Kim, Jiheong Kang, Helen Tran, Hung-Chin Wu, Insang You, Zhenan Bao, and Xiaodong Chen**

Dr. N. Matsuhisa, Ms. Y. Jiang, Dr. Z. Liu, Ms. G. Chen, Dr. C. Wan, Prof. X. Chen
Innovative Centre for Flexible Devices (iFLEX), School of Materials Science and
Engineering, Nanyang Technological University, 50 Nanyang Avenue, 639798, Singapore
Email: chenxd@ntu.edu.sg
Webpage: <http://www.ntu.edu.sg/home/chenxd>

Dr. N. Matsuhisa, Dr. Y. Kim, Dr. J. Kang, Dr. H. Tran, Dr. H.-C. Wu, Mr. Insang You, Prof.
Z. Bao
Department of Chemical Engineering, Stanford University, Stanford, CA 94305, USA

Keywords: Stretchable electronics, Organic electrochemical transistors, Stretchable
conductors

Abstract

High-transconductance stretchable transistors are important for conformable and sensitive sensors for wearables and soft robotics. Remarkably high transconductance to enable large amplification of signals has been achieved by organic electrochemical transistors (OECTs). However, its stretchability has been tempered by the lack of stretchable conductors with high stability in electrolytes, high conductance at high strain (100%), and process compatibility with the active layers. Here, we demonstrate highly stretchable and strain-resistant Au conductors which were employed to fabricate intrinsically stretchable OECTs. Notably, our Au conductors possessed a sheet resistance of 33.3 $\Omega/\text{Sq.}$ at 120% strain, the lowest reported value to date among stretchable Au thin film conductors. High-performance stretchable Au was realized by suppressing strain-induced microcrack propagation through control of the microcracks formed in the as-deposited Au thin films. Then, the highly stretchable Au conductors were utilized to fabricate intrinsically stretchable OECTs with a high transconductance both at 0% strain (0.54 mS) and 140% strain (0.14 mS). Among previously reported literature, our OECTs showed the highest transconductance at high strain (>50%).

Finally, the high performance OECTs were utilized in stretchable synaptic transistors, which are critically important for the development of soft neuromorphic computing systems to provide artificial intelligence for future soft robotics.

Main text

1. Introduction

Highly sensitive and soft electronic transducers enable sensing of mechanical, chemical, and electrical signals with high fidelity.^[1–4] Such devices are important for next-generation healthcare applications and robotics.^[5–7] Organic electrochemical transistors (OECTs) are the building block of many of the most sensitive sensors.^[8,9] Unlike conventional field effect transistors (FETs), OECTs consists of an active layer with mixed electronic and ionic transport, enabling remarkably high transconductance (g_m) for high amplification of signals.^[10,11] For example, OECT-based devices for electrophysiological recording with high signal integrity,^[8,9,12] highly sensitive biosensors,^[13–16] neuromorphic applications,^[17] display drivers,^[18] and optical logic gates^[19] have been reported. However, practical applications of OECTs critically rely on the development of devices with a high transconductance at high strain ($\sim 100\%$) to accommodate for the dynamic range of motions and shapes of the human body.^[20] The breakdown of high transconductance typically stems from the high resistance of the source/drain electrodes at high strain. Electrodes must be highly conductive at high strain, stable in the electrolyte, and soft enough to avoid stress concentration at the interface with the active layer.^[21,22] While there have been reports of highly conductive stretchable conductors (Ag-based materials, carbon nanotubes, and liquid metals ^[3,23–27]), there has yet been a demonstration of a stretchable conductor which collectively satisfies the aforementioned requirements. Importantly, plain Au thin films are not stretchable while Au thin films with microcrack morphology are stretchable and electrolyte-stable.^[28–32] However, the conductance at high strain ($\sim 100\%$) was not ideal, with sheet resistance increasing over two orders of

magnitude observed due to the large strain-induced microcrack propagation. This large microcrack propagation originates from the uncontrolled morphology of initial microcracks in as-deposited Au thin films. We propose that control over the initial microcrack morphology and propagation may lead to improved and stable conductance at high strains.

Here, we report highly stretchable ($\sim 140\%$) and high-transconductance (>0.1 mS) OECTs, enabled by microcracked Au conductors engineered by programming the initial microcrack formation (**Figure 1a**). Inspired by kirigami-structures, we hypothesized that highly stretchable Au can be obtained if the initial microcracks of Au film have high aspect ratios. We have two parameters to control the growth mode of Au and hence the resulting microcracks: evaporation rate and film thickness. By depositing 40 nm thick Au on an elastomeric substrate at a high evaporation rate (32 \AA/s), we fabricated highly stretchable microcracked Au with a low sheet resistance of $11.8 \text{ } \Omega/\text{Sq.}$ at 0% strain, which minimally increased to $33.3 \text{ } \Omega/\text{Sq.}$ at 120% strain. In contrast, microcracked Au thin films fabricated by previously reported methods (evaporated at 0.5 \AA/s) showed a sheet resistance of $12.4 \text{ } \Omega/\text{Sq.}$ at 0% strain, and a noticeably larger sheet resistance of $101.5 \text{ } \Omega/\text{Sq.}$ at 120% strain. Furthermore, the high performance of our system was maintained over 10^4 cycles at 50% strain and over 10^3 cycles at 100% strain. OECTs employing this highly stretchable Au showed high g_m of 0.54 mS at 0%, and 0.14 mS at 140% strain, which is the highest value in intrinsically stretchable transistors, to the best of our knowledge. Moreover, the transconductance remained as high as 0.24 mS over 10^3 cycles at 50% strain. The high performance stretchable OECTs were ideally suited for the fabrication of highly stretchable synaptic transistors. The high transconductance synaptic transistor is a crucial component to construct neuromorphic computing systems for next generation wearables and soft robotics.

2. Highly stretchable microcrack Au conductors

We postulated that the initial microcrack formation in Au thin films plays an important role in reducing the resistance change against strain, as described in Figure 1b-e. In previously reported stretchable Au conductors with the microcrack morphology, the initial length along the long axis of each microcrack was low ($<2\text{ }\mu\text{m}$). These short microcracks may easily propagate into longer microcracks which subsequently disrupt conducting pathways (Figure 1b, c). On the other hand, long initial microcracks ($>8\text{ }\mu\text{m}$) can accommodate larger strains, thus suppressing rapid microcrack propagation (Figure 1d and e). Therefore, reduced resistance change by strain was expected.

2.1. Simulations of Au thin films with different fractures

This hypothesis was first verified by two-dimensional finite element analysis (2D FEA) simulations of thin films with short and long fracture types (Figure 1f and g, respectively). Two advantageous effects on the stress relaxation was observed for the long fracture type. First, suppressed stress concentration at the tip of cracks for long fractures were observed compared to the tip of cracks for short fractures under the same strain. This was quantitatively described by the J-integral, which represents the energy dissipated at the fracture site (Figure S1a-c). Second, more stress relaxation in the surrounding area was observed for the long fractures compared with short fractures (Figure S1d-f). The J-integral at the tip of small fracture next to the main long fracture was significantly smaller (over two orders of magnitude) when compared to the similar calculation with a main short fracture. Thus, we infer from the simulations that films with short microcracks undergo uniform strain, resulting in microcrack propagation over the entire Au thin film. On the other hand, most of the strain in the films with long microcracks is used to widen the long microcracks as opposed to microcrack propagation, preserving the conducting pathways at high strain.

2.2. Control of Au microcrack morphology

Experimentally, the longer microcrack lengths (or higher aspect ratios) in the Au thin films were achieved by depositing Au at higher rates compared to previously reported conditions. Au films with a thickness of 40 nm were thermally deposited with 3-nm Cr adhesion layers on 100- μm -thick crosslinked polydimethylsiloxane (PDMS) substrates. PDMS was chosen as the substrate because of its ease of processability, high elasticity, and biocompatibility.^[31] As shown in the scanning electron microscope (SEM) images in **Figure 2a** and **e**, longer microcrack formation was observed for Au thin films deposited at 32 $\text{\AA}/\text{s}$ compared to thin films deposited at 0.5 $\text{\AA}/\text{s}$. Evaporation rates higher than 32 $\text{\AA}/\text{s}$ were not tested due to the power limitation of our evaporator. SEM images of initial microcracks deposited at 2.0 and 8.0 $\text{\AA}/\text{s}$ are shown in Figure S2. Image analysis of these SEM images illustrate the trend of increasing maximum initial microcrack length with increasing evaporation rates: 1.4 μm (0.5 $\text{\AA}/\text{s}$) to 8.8 μm (32 $\text{\AA}/\text{s}$) (Figure 2i, S3). The total number of initial microcracks was not affected by the evaporation rate. The root mean square (RMS) roughness of Au thin films deposited at 0.5 and 32 $\text{\AA}/\text{s}$ was 7.96 and 19.48 nm, respectively, reflecting the change in microcrack morphology (Figure S4). Notably, while control of Au morphology (plain, microcrack, or buckled) by substrate temperature and surface energy was previously reported, this is the first report to deliberately control the length of initial microcracks which directly impacts the performance of the stretchable conductor.^[32]

The initial microcrack formation showed a strong influence on the microcrack propagation upon stretching. Figure 2b, c, and Figure 2f, g show the SEM images of Au films deposited at an evaporation rate of 0.5 $\text{\AA}/\text{s}$, and 32 $\text{\AA}/\text{s}$, respectively, and then stretched to 100% strain. Image analysis of the SEM images show the distribution of microcrack lengths at 100% strain (Figure 2j). Au films evaporated at 32 $\text{\AA}/\text{s}$ showed less microcrack propagation (maximum microcrack length at 100% strain/ maximum initial microcrack length) than those with low

deposition rates, indicating that the original conducting pathways were better maintained. The microcrack propagation at 100% strain was as high as 41 for Au films deposited at 0.5 Å/s, and only 5 for those at 32 Å/s. In addition, Au films deposited at 32 Å/s showed twice as many microcracks as those at 0.5 Å/s. This suggests that microcracks in Au films deposited at 0.5 Å/s propagated and merged into long microcracks to meander their conducting pathways while Au films deposited at 32 Å/s maintained the original conducting pathways. Additionally, Figure S5 shows SEM images of Au films with different evaporation rates (0.5, 2.0, 8.0, 32 Å/s), and different strains (20, 50, 100%). Image analysis further supports the trend that smaller microcrack propagation was observed in Au films deposited at higher evaporation rates than those at lower evaporation rates and microcrack propagation was exacerbated at higher strains (Figure S6). This observation was in agreement with the simulation (Figure 1f,g and Figure S1a-c). Furthermore, the propagation of small microcracks surrounding long microcracks was suppressed (Figure 2f), which also matches with our simulation in Figure S1d-f.

2.3. Electrical properties

Au films with small microcrack propagation showed significantly lower sheet resistance at high strain (>100%). Figure 2k shows the sheet resistance versus strain characteristics of Au films with different deposition rates (0.5, 2.0, 8.0, and 32 Å/s). For all depositions rates, the initial sheet resistance was ~12 Ω/Sq. At 120% strain, the sheet resistance was significantly reduced from 101.5 Ω/Sq. to 33.3 Ω/Sq. when the deposition rate increased from 0.5 to 32 Å/s (additional evaporation rates shown in Figure S7). Notably, an evaporation rate higher than 4 Å/s significantly reduced sheet resistance at high strain. The thickness of evaporated Au also influenced the initial microcrack length and consequently the conductance at high strain (Figure S8). When the thickness of Au was thin (20 and 40 nm), the number of long initial microcracks was larger than those for Au films with thicknesses of 60 and 80 nm (Figure S8a-

e, SEM images and the image analysis). Thus, the resistance change of thick Au films (60, 80 nm) became greater than that of thinner Au films (20, 40 nm) upon stretching (Figure S8f). Smaller numbers of long initial microcracks were obtained in thick Au films because evaporated Au can fill the gaps in microcracks. Au films with a thickness of 20 nm showed high sheet resistance ($\sim 100 \text{ } \Omega/\text{Sq.}$) because Au did not form a fully percolated thin film.

The low sheet resistance at high strain was further verified by voltage distribution analysis of the SEM images (Figure 2d,h).^[33,34] In this analysis, virtual voltage was applied along the stretching direction to the percolating network of Au in SEM images, and the voltage distribution was visualized. In the highly stretchable Au (evaporation rate of $32 \text{ } \text{\AA}/\text{s}$), the size of microcracks remained small upon 100% strain, and contiguous conducting pathways were maintained (Figure 2h). On the other hand, in the stretchable Au deposited at an evaporation rate of $0.5 \text{ } \text{\AA}/\text{s}$, microcrack propagation resulted in disruptions to the conducting pathways, yielding faster voltage drops across the Au microcracks (Figure 2d). Sheet resistance change by strain was calculated from these images, demonstrating Au films deposited at high rate show smaller change in resistance compared with those at low rate. This trend was consistent with our experimental results (Figure S9).

Figure S10a compares previously reported stretchable Au on elastomeric substrates^[28,30,35] with our system, clearly showing that our programmed microcracked Au displays substantially reduced sheet resistance upon strain. In fact, that sheet resistance of our stretchable Au conductor is 40 times lower than a recently reported method based on flash deposition ($>200 \text{ } \text{\AA}/\text{s}$) in low vacuum.^[35] Their microcrack length at 50% strain was larger than $50 \text{ } \mu\text{m}$, which is much larger than those reported here. In our study, we carefully tuned the evaporation rate and thickness to systematically control the formation of initial Au microcracks. Furthermore, our stretchable Au showed a sheet resistance comparable to Au on

the surface of structured elastomers (e.g. micropillars) which rely on physical barrier to inhibit crack propagation (Figure S10b).^[35–39] Importantly, our stretchable Au does not require a rough surface, or any additional processes such as molding,^[36,40] or pre-strain,^[38] which preserves the high compatibility with traditional thin film device processing.

Our stretchable Au showed high durability against cyclic strain. SEM images of microcracked Au films after 1000 cycles at 100% strain are shown in Figure S11a, c, evaporated at a rate of 32 Å/s, and 0.5 Å/s, respectively. Both films showed vertical and lateral microcracks relative to the stretching direction, which is consistent with a previous report.^[30] Even after such a large number of cycles, Au microcracked films evaporated at 32 Å/s displayed shorter microcrack lengths with continuous conducting pathways than those at 0.5 Å/s, which was attributed to the limited microcrack propagation. This difference was directly correlated with the electrical performance (Figure 21). After 1000 cycles of 100% strain, the Au microcracked films deposited at 32 Å/s showed a sheet resistance of 19.0 Ω/sq. (0% strain), and 28.0 Ω/sq. (100% strain). On the other hand, after 1000 cycles of 100% strain, Au microcracked films deposited at 0.5 Å/s showed the sheet resistance of 33.1 Ω/sq. (0% strain), and 60.3 Ω/sq. (100% strain). Au microcracked films evaporated at 32 Å/s showed lower resistance at both 0% and 100% strain, and they were more robust against cycling, as evidenced by the lower slopes in the sheet resistance versus cycle number (dashed lines in Figure 21). Sheet resistance of Au films deposited at 0.5 Å/s increased by 1.6 Ω/sq. per 100 cycles (0% strain), and 1.7 Ω/sq. per 100 cycles (100% strain). On the other hand, sheet resistance of Au films deposited at 32 Å/s showed 0.3 Ω/sq. per 100 cycles (0% strain) and 0.9 Ω/sq. per 100 cycles (100% strain). Similarly, the Au microcracked films deposited at 32 Å/s showed improved performance relative to the Au deposited at 0.5 Å/s in 1,000 cycles of 50% strain due to the suppressed microcrack propagation (Figure S12). After 1000 cycles of 50% strain, the Au microcracked films deposited at 32 Å/s showed a sheet resistance of 13.4 Ω/Sq. (0% strain)

and 13.8 Ω/Sq . (50% strain). On the other hand, the Au microcracked films deposited at 0.5 $\text{\AA}/\text{s}$ showed a sheet resistance of 16.7 Ω/Sq . (0% strain) and 29.9 Ω/Sq . (50% strain). Furthermore, Au microcracked films deposited at 32 $\text{\AA}/\text{s}$ showed high durability even against 10,000 cycles at 50% strain, exhibiting a sheet resistance of 19.2 Ω/Sq . at 0% strain and 25.7 Ω/Sq at 50% strain. (Figure S13).

The initial microcrack formation was investigated by observing the growth mode of Au microcracked thin films with different evaporation rates. Figure S14 shows Au microcracked thin films with a thickness of 10, 20, and 40 nm, deposited at evaporation rates of 0.5 and 32 $\text{\AA}/\text{s}$. When deposited at 0.5 $\text{\AA}/\text{s}$, small Au particles were uniformly formed. On the contrary, when deposited at 32 $\text{\AA}/\text{s}$, the Au particles coalesced and formed more apparent grain boundaries manifested as microcracks, in agreement with previous studies on the dependence of Au thin film growth mode with different evaporation rates.^[41–43] The interplay between grain boundary size and evaporated Au film thickness is shown in Figure S14a-c, where the microcracks become extended at 20 nm and the width of the microcracks become wider at 40 nm. An increase in Au film thickness from 10 nm to 40 nm correlates to a larger size of grain boundaries. We also confirmed that Ag thin films can be made stretchable and conductive with microcracked morphology (Figure S15). Additionally, we note that the thermal expansion mismatch between Au and PDMS may also play a role in the initial crack formation, and the optimal condition for achieving similar long microcracks on other elastomeric substrates may vary. In our experiment, substrate temperature was fixed to 23 $^{\circ}\text{C}$ (room temperature) by substrate cooling unit, because high substrate temperature during deposition can result in non-microcracked Au morphology.^[32] In addition, the distance between substrates and an evaporation source was set to as far as 30 cm for high reproducibility.

3. Stretchable organic electrochemical transistors

3.1. Stretchability of the active layer

The stretchable microcracked Au is well suited as electrode interconnects for intrinsically stretchable OECTs owing to its inertness and high conductance. Intrinsically stretchable OECTs were fabricated, as described in the Experimental Section. **Figure 3a-d** show the experimental setup and optical microscopy images of the devices. We verified that the high performance of the microcracked Au thin films was maintained with 150% strain when patterned from 2 mm down to 100 μm line widths via shadow masking (Figure S16). PEDOT:PSS crosslinked by (3-glycidyloxypropyl) trimethoxysilane (GOPS) was selected as the active layer because of its high performance arising from dual ion and electron conduction.^[11] Dry, pristine PEDOT:PSS films possesses limited stretchability (5% strain),^[44,45] and showed a large number of film fractures at a strain of 50% (Figure S17). The stretchability of PEDOT:PSS was improved due to swelling by electrolytes and a reduced amount of GOPS (0.1 vol% in solution instead of 1.0 vol% in solution). The stretchability of PEDOT:PSS improved because the electrolytes effectively serve as plasticizers. At 100% strain, film fractures were observed when the GOPS concentration was 1.0 vol% (Figure 3e), which is the commonly adopted amount for OECTs.^[9,12] Here, we found that stretchability higher than 100% was obtained when the GOPS concentration was as low as 0.1 vol% (Figure 3d), which is a sufficient amount to render PEDOT:PSS insoluble in water.^[46]

3.2. Electrical properties

The high stretchability of our intrinsically stretchable OECTs was confirmed by measuring OECTs upon 140% strain. Figure 3f and g show the $-I_d$ - V_g curves, and g_m at different strains, respectively. Without strain, the $-I_d$ was as high as 0.25 mA (at $V_g = V_d = -0.6$ V), and the g_m was as high as 0.54 mS, which were consistent with previous reports when considering the volume of the active layer.^[12,47] When the devices were stretched, the g_m increased to 0.64 mS

at 10% strain and decreased to 0.14 mS at 140% strain. To date, this is the highest g_m reported among intrinsically stretchable transistors with a strain of 50-140% (Figure 3g).^[21,22,48–53] It is important to note that the highly stretchable microcracked Au that we developed enabled the high performance of these OECTs at high strain. Stretchable OECTs have been reported by prestretching substrate during the fabrication,^[22] or serpentine-structured stretchable interconnects.^[21] However, the stretchability was limited to ~40% due to the high resistance of source/drain electrodes or stress concentration at the interface of substrate and stiff serpentine structured electrodes. At all strains up to 140%, the resistance of our highly stretchable microcracked Au was insignificant and did not affect the I_d , which was confirmed by comparing the resistance of OECT (I_d/V_d) with the resistance of Au wire (Figure S18). The microcracked Au deposited at 32 Å/s had resistance one-twentieth as low as the total resistance of the OECT. On the other hand, microcracked Au deposited at 0.5 Å/s showed a resistance higher than one-tenth resistance of OECT, which can adversely influence the overall performance of OECT. The effect of sheet resistance would be more significant when OECTs are fabricated in high resolutions or array because of the requirement for the thin and long wires to access to each device. In addition, our stretchable Au conductors do not influence the stiffness of whole device, so the device is free from stress concentration at the interface of soft and rigid materials.

The increase of g_m at 10% strain may be attributed to the chain alignment of PEDOT:PSS.^[45] The decrease of g_m at strains higher than 20% mainly arise from a geometrical change of the channels (e.g., thickness, and W/L). When the I_d was normalized by strain, it showed stable performance (Figure S19). The performance of OECTs fabricated with GOPS concentration of 1.0 vol% diminished at 70% strain, which was consistent with the observed fractured PEDOT:PSS films at 100% strain shown in Figure 3e. Furthermore, the device showed high cyclic durability. After 10, 100, and 1000 cycles of 50% strain, the g_m was kept as high as

0.38, 0.29, and 0.24 mS, respectively (Figure S20). The relatively low on-off ratio (~ 3) does not necessarily limit the application to amplify the signals input to the transistors because the voltage of such input signals is typically low and the transconductance (amplification) is kept high. The change of active materials formulation or operation voltage did not improve the on-off ratio (Figure S21). We attributed this suppressed on-off ratio to the electrostatics of the elastomeric substrates. Charges in the substrate could disturb the gating of active materials.

3.3. Stretchable synaptic transistors

This intrinsically stretchable and high performance OECT by our highly stretchable Au conductors enabled the fabrication of a stretchable synaptic transistor (**Figure 4**). A synaptic transistor is a building block for neuromorphic computation system, which is ultra-low power, plastic, and fault-tolerant similar to the brain of human beings.^[6,54,55] Synaptic plasticity is believed to be one of the fundamental mechanisms that underlie memory and learning behaviors, and it is related to encoding temporal stimuli with facilitating or inhibitory manners.^[56] Paired-pulse facilitation (PPF), an important form of short-term plasticity, has been intensively mimicked by a broad spectrum of synaptic devices.^[57,58] The advantage of this function has been demonstrated by *in situ* signal processing in flexible sensor applications.^[59,60] In our measurement, paired spikes with different temporal intervals were applied to the synaptic transistors, and the ratio of two peaks of the output signal was evaluated as PPF index. Figure 4c shows the PPF of our OECTs with 0 and 100% strain, and their PPF index is shown in Figure 4d. Integration of two signals and larger PPF index were obtained, which is consistent with previous reports on synaptic devices, with 0 and 100% strain. The stretchable synaptic devices developed here may serve as a fundamental building block for developing soft neuromorphic computing systems which may provide artificial intelligence for future soft robotics.

4. Conclusion

In conclusion, we have demonstrated intrinsically stretchable OECTs by the development of highly stretchable microcracked Au. The highly stretchable microcracked Au was realized by controlling the initial Au microcrack length on the elastomeric substrate, where high evaporation rates yielded high conductivity even at 100% strain. The high conductance of our system extends the range of stretchability and size in many applications, such as wearable or implantable electronic devices, and devices for cell culturing.^[31,61,62] Moreover, our highly stretchable OECTs possess high stretchability as well as high transconductance. These stretchable OECTs would realize high sensitivity in conformable sensors for electrophysiology, or biological markers while achieving less wear discomfort, and stretchable neuromorphic devices for signal processing in future soft robotics.

5. Experimental Section

2D FEA simulation: FEA was employed to analyze the stress distribution around the Au microcracks. The entire model was built using 2D shell planar features, under planar stress. A representative unit containing multiple cracks were simulated to explore the stress distribution in the presence of neighboring cracks. The Au thin film was modeled as an isotropic elastic material, with a Young's modulus of 80 GPa and Poisson's ratio of 0.42. The boundary conditions were set as 10% nominal strain in the stretching direction, and free in the transverse direction, which is consistent with boundary conditions in the experiment.

Stretchable microcrack Au fabrication: 100- μ m-thick PDMS substrates were prepared by spincoating PDMS precursor (Sylgard 184, Dow Corning) on fluorinated Si/SiO_x substrate at 800 rpm for 40 s. PDMS precursor was prepared by mixing the prepolymer and crosslinking agent (weight ratio of 10:1). The other weight ratios (*e.g.*, 20:1, 30:1) were not tested to avoid the effect of uncrosslinked residues and different surface energies which can influence the Au

film formation.^[63,64] After spincoating, samples were cured at 60 °C for >12 h. After deposition of 3-nm Cr at evaporation rate of 0.1 Å/s, Au was evaporated using a tungsten boat (2.00" Dia. × 0.125" Thick 99.95%, Kurt. J. Lesker), Au bullet (purity: >99.9%, Kurt. J. Lesker), and thermal vacuum evaporator (Nano 36, Kurt. J. Lesker) under vacuum pressure of $<1.0 \times 10^{-4}$ Pa. The distance between the evaporation source and samples was fixed to 30 cm. The sample holder was rotating during evaporation, and uniform metal thin films were obtained within the size of the sample holder (diameter: >15 cm). Sample stage temperature was set to 23°C by the substrate chiller. The substrate temperature was expected to be constant because of this chiller system, and the evaporation time was very short (~10 s) when Au was evaporated at a high deposition rate. Still, the surface of the substrate can be slightly heated by the radiation from the evaporation source, which can induce the microcrack formation after the deposition. The evaporation speed was controlled from 0.5 Å/s to 32 Å/s by the program for high reproducibility. When necessary, metal shadow masks were used for patterning.

SEM observation and the image analysis: SEM images were taken by JSM6340F, JEOL without any surface coatings. In order to fix the samples under strain, carbon tape was used. All the image analysis was carried out using the Fiji software. The number and length of microcracks were counted by the following steps (described in Figure S3). 1: Bandpass filtering images (3-40 pixels) for highlighting the edges of microcracks. 2: Binarizing for detecting microcracks. SEM images of the stretched samples were binarized under the assumption that the area of Au films does not change and all the strain was applied to microcracked regions. 3: Skeletonizing in order to remove the information of microcrack width. 4: After these image processing, each area of the particles (the black part in Figure S3d) corresponds to the microcrack length. Due to the microcrack size differences, SEM images with a magnification of $\times 5k$ were used for analyzing images without strain, and $\times 2k$

were used for with strains. Voltage simulation analysis was carried out following our previous study after the binarization.^[34] Based on this voltage simulation analysis, resistance change (R/R_0) was calculated.

Electrical measurement while stretching: Resistance-strain characteristics were measured using a semiconductor parameter analyzer (Keithley 4200, Tektronix) while being stretched by manual stretcher. The samples were cut into 2 cm (length) \times 1 cm (width) when there was no Au patterning by shadow masks. The electrical contact to microcrack Au was made by liquid metal (eutectic GaIn, Sigma Aldrich), and thin copper wires. The cyclic strain was applied using a mechanical tester (C42, MTS Systems Corporation). Sheet resistance was calculated with an assumption that the total area of Au did not change with strain, and the substrate was isotopically deformed in thickness and width while keeping the total volume the same. For comparisons with the previous studies which do not show sheet resistance-strain characteristics, it was calculated based on the resistivity, dimensions (thickness, width, and length), and resistance change (R/R_0) with the aforementioned assumptions.

Fabrication and measurement of stretchable OECTs: Microcrack Au was first formed by the above procedure. The source/drain contacts and wires were defined by metal shadow masks. The width and length of the channel were 630 and 130 μm , respectively. The width of the wiring part for source and drain contacts were 5 mm. For the patterning of the active layer, the wettability of the substrates was modified by O_2 plasma treatment (Power: 30%, Duration: 30 s, Diener electronic) and metal shadow masks. The active layer ink was then spincoated at 3000 rpm for 60 s. The ink was prepared by mixing highly conductive PEDOT:PSS (PH1000, Clevious), ethylene glycol, GOPS, and dodecylbenzene sulfonic acid (DBSA) in the ratio of 1000:50:1:1 (0.1 vol% GOPS) or 1000:50:10:1 (1.0 vol% GOPS) (v:v:v:v). In addition, the inks were sonicated for 10 min. and filtered with a polyvinylidene fluoride syringe filter with

a pore size of 0.45 μm . The active layer was cured at 150°C for 30 min. The OECTs were measured using electrolytes of 100 mM NaCl deionized water solution, gate electrodes of Ag/AgCl, and a semiconductor parameter analyzer while strain was applied using a manual stretch station. The comparison of g_m was made by extracting the value from the g_m -strain characteristics or I_d - V_g characteristics.

Supporting Information

Supporting Information is available from the Wiley Online Library or from the author.

Acknowledgements

The authors thank the financial support from the National Research Foundation, Prime Minister's office, Singapore, under its NRF Investigatorship (NRF2016NRF-NRF1001-21), the Singapore Ministry of Education (MOE2015-T2-2-60). N.M. was supported by Japan Society for the Promotion of Science (JSPS) overseas research fellowship. H.T. was supported by an appointment to the Intelligence Community Postdoctoral Research Fellowship Program at Stanford University administered by Oak Ridge Institute for Science and Education through an interagency agreement between the U.S. Department of Energy and the Office of the Director of National Intelligence.

Conflict of Interest

The authors declare no conflict of interest.

Received: ((will be filled in by the editorial staff))

Revised: ((will be filled in by the editorial staff))

Published online: ((will be filled in by the editorial staff))

References

- [1] T. Sekitani, T. Yokota, K. Kuribara, M. Kaltenbrunner, T. Fukushima, Y. Inoue, M. Sekino, T. Isoyama, Y. Abe, H. Onodera, T. Someya, *Nat. Commun.* **2016**, 7, 11425.
- [2] D.-H. Kim, N. Lu, R. Ma, Y.-S. Kim, R.-H. Kim, S. Wang, J. Wu, S. M. Won, H. Tao, A. Islam, K. J. Yu, T.-I. Kim, R. Chowdhury, M. Ying, L. Xu, M. Li, H.-J. Chung, H. Keum, M. McCormick, P. Liu, Y.-W. Zhang, F. G. Omenetto, Y. Huang, T. Coleman,

- J. A. Rogers, *Science* **2011**, 333, 838.
- [3] D. J. Lipomi, M. Vosgueritchian, B. C.-K. Tee, S. L. Hellstrom, J. a Lee, C. H. Fox, Z. Bao, *Nat. Nanotechnol.* **2011**, 6, 788.
- [4] W. Gao, S. Emaminejad, H. Y. Y. Nyein, S. Challa, K. Chen, A. Peck, H. M. Fahad, H. Ota, H. Shiraki, D. Kiriya, D. Lien, G. A. Brooks, R. W. Davis, A. Javey, *Nature* **2016**, 529, 509.
- [5] B. C.-K. Tee, A. Chortos, A. Berndt, A. K. Nguyen, A. Tom, A. McGuire, Z. C. Lin, K. Tien, W.-G. Bae, H. Wang, P. Mei, H.-H. Chou, B. Cui, K. Deisseroth, T. N. Ng, Z. Bao, *Science* **2015**, 350, 313.
- [6] Y. Kim, A. Chortos, W. Xu, Y. Liu, J. Y. Oh, D. Son, J. Kang, A. M. Foudeh, C. Zhu, Y. Lee, S. Niu, J. Liu, R. Pfattner, Z. Bao, T.-W. Lee, *Science* **2018**, 360, 998.
- [7] M. Kaltenbrunner, T. Sekitani, J. Reeder, T. Yokota, K. Kuribara, T. Tokuhara, M. Drack, R. Schwödiauer, I. Graz, S. Bauer-Gogonea, S. Bauer, T. Someya, *Nature* **2013**, 499, 458.
- [8] D. Khodagholy, T. Doublet, P. Quilichini, M. Gurfinkel, P. Leleux, A. Ghestem, E. Ismailova, T. Hervé, S. Sanaur, C. Bernard, G. G. Malliaras, *Nat. Commun.* **2013**, 4, 1575.
- [9] W. Lee, D. Kim, N. Matsuhisa, M. Nagase, M. Sekino, G. G. Malliaras, T. Yokota, T. Someya, *Proc. Natl. Acad. Sci.* **2017**, 114, 10554.
- [10] D. Khodagholy, J. Rivnay, M. Sessolo, M. Gurfinkel, P. Leleux, L. H. Jimison, E. Stavriniidou, T. Herve, S. Sanaur, R. M. Owens, G. G. Malliaras, *Nat. Commun.* **2013**, 4, 2133.
- [11] J. Rivnay, S. Inal, B. A. Collins, M. Sessolo, E. Stavriniidou, X. Strakosas, C. Tassone, D. M. DeLongchamp, G. G. Malliaras, *Nat. Commun.* **2016**, 7, 11287.
- [12] W. Lee, D. Kim, J. Rivnay, N. Matsuhisa, T. Lonjaret, T. Yokota, H. Yawo, M. Sekino, G. G. Malliaras, T. Someya, *Adv. Mater.* **2016**, 28, 9722.

- [13] D. Khodagholy, V. F. Curto, K. J. Fraser, M. Gurfinkel, R. Byrne, D. Diamond, G. G. Malliaras, F. Benito-Lopez, R. M. Owens, *J. Mater. Chem.* **2012**, 22, 4440.
- [14] N. Y. Shim, D. Bernards, D. Macaya, J. DeFranco, M. Nikolou, R. Owens, G. Malliaras, *Sensors* **2009**, 9, 9896.
- [15] G. Scheiblin, R. Coppard, R. M. Owens, P. Mailley, G. G. Malliaras, *Adv. Mater. Technol.* **2017**, 2, 1.
- [16] P. Lin, F. Yan, J. Yu, H. L. W. Chan, M. Yang, *Adv. Mater.* **2010**, 22, 3655.
- [17] P. Gkoupidenis, N. Schaefer, B. Garlan, G. G. Malliaras, *Adv. Mater.* **2015**, 27, 7176.
- [18] P. Andersson, D. Nilsson, P.-O. Svensson, M. Chen, A. Malmström, T. Remonen, T. Kugler, M. Berggren, *Adv. Mater.* **2002**, 14, 1460.
- [19] B. Kolodziejczyk, C. H. Ng, X. Strakosas, G. G. Malliaras, B. Winther-Jensen, *Mater. Horizons* **2018**, 5, 93.
- [20] Y. Menguc, Y.-L. Park, H. Pei, D. Vogt, P. M. Aubin, E. Winchell, L. Fluke, L. Stirling, R. J. Wood, C. J. Walsh, *Int. J. Rob. Res.* **2014**, 33, 1748.
- [21] B. Marchiori, R. Delattre, S. Hannah, S. Blayac, M. Ramuz, *Sci. Rep.* **2018**, 8, 8477.
- [22] S. Zhang, E. Hubis, G. Tomasello, G. Soliveri, P. Kumar, F. Cicoira, *Chem. Mater.* **2017**, 29, 3126.
- [23] N. Matsuhisa, D. Inoue, P. Zalar, H. Jin, Y. Matsuba, A. Itoh, T. Yokota, D. Hashizume, T. Someya, *Nat. Mater.* **2017**, 16, 834.
- [24] J. Liang, K. Tong, Q. Pei, *Adv. Mater.* **2016**, 28, 5986.
- [25] M. D. Dickey, *Adv. Mater.* **2017**, 29, 1606425.
- [26] X. Chen, *Small Methods* **2017**, 1, 1600029.
- [27] M. Park, J. Im, M. Shin, Y. Min, J. J. Park, H. Cho, S. Park, M.-B. Shim, S. Jeon, D.-Y. Chung, J. Bae, J. J. Park, U. Jeong, K. Kim, *Nat. Nanotechnol.* **2012**, 7, 803.
- [28] C. Tsay, S. P. Lacour, S. Wagner, T. Li, Z. Suo, in *Mater. Res. Soc. Symp. Proc.*, **2005**, p. O5.5.

- [29] S. P. Lacour, D. Chan, S. Wagner, T. Li, Z. Suo, *Appl. Phys. Lett.* **2006**, 88, 204103.
- [30] I. M. Graz, D. P. J. Cotton, S. P. Lacour, *Appl. Phys. Lett.* **2009**, 94, 071902.
- [31] I. R. Mineev, P. Musienko, A. Hirsch, Q. Barraud, N. Wenger, E. M. Moraud, J. Gandar, M. Capogrosso, T. Milekovic, L. Asboth, R. F. Torres, N. Vachicouras, Q. Liu, N. Pavlova, S. Duis, A. Larmagnac, J. Voros, S. Micera, Z. Suo, G. Courtine, S. P. Lacour, *Science* **2015**, 347, 159.
- [32] O. Graudejus, P. Görrn, S. Wagner, *ACS Appl. Mater. Interfaces* **2010**, 2, 1927.
- [33] W. Cao, P. Görrn, S. Wagner, *Appl. Phys. Lett.* **2011**, 98, 40.
- [34] Y. Jiang, Z. Liu, N. Matsuhisa, D. Qi, W. R. Leow, H. Yang, J. Yu, G. Chen, Y. Liu, C. Wan, Z. Liu, X. Chen, *Adv. Mater.* **2018**, 30, 1706589.
- [35] V. Venugopalan, R. Lamboll, D. Joshi, K. S. Narayan, *ACS Appl. Mater. Interfaces* **2017**, 9, 28010.
- [36] P. Mandlik, S. P. Lacour, J. W. Li, S. Y. Chou, S. Wagner, *IEEE Electron Device Lett.* **2006**, 27, 650.
- [37] H. L. Filiatrault, R. S. Carmichael, R. A. Boutette, T. B. Carmichael, *ACS Appl. Mater. Interfaces* **2015**, 7, 20745.
- [38] S. Moon, H. K. Park, J. H. Song, S. Cho, J. C. J. Kim, J. C. J. Kim, H. Hwang, H. S. Kim, U. Jeong, **2018**, 1801408, 1.
- [39] G. Chen, N. Matsuhisa, Z. Liu, D. Qi, P. Cai, Y. Jiang, C. Wan, Y. Cui, W. R. Leow, Z. Liu, S. Gong, K.-Q. Zhang, Y. Cheng, X. Chen, *Adv. Mater.* **2018**, 30, 1800129.
- [40] Z. Liu, X. Wang, D. Qi, C. Xu, J. Yu, Y. Liu, Y. Jiang, B. Liedberg, X. Chen, *Adv. Mater.* **2017**, 29, 1603382.
- [41] Z. H. Liu, N. M. D. Brown, A. McKinley, *J. Phys. Condens. Matter* **1997**, 9, 59.
- [42] D. Qi, Z. Liu, M. Yu, Y. Liu, Y. Tang, J. Lv, Y. Li, J. Wei, B. Liedberg, Z. Yu, X. Chen, *Adv. Mater.* **2015**, 27, 3145.
- [43] T. Tsujioka, Y. Sesumi, R. Takagi, K. Masui, S. Yokojima, K. Uchida, S. Nakamura, *J.*

- Am. Chem. Soc.* **2008**, *130*, 10740.
- [44] D. Lipomi, J. Lee, *Chem. Mater.* **2012**, *24*, 373.
- [45] Y. Wang, C. Zhu, R. Pfattner, H. Yan, L. Jin, S. Chen, F. Molina-Lopez, F. Lissel, J. Liu, N. I. Rabiah, Z. Chen, J. W. Chung, C. Linder, M. F. Toney, B. Murmann, Z. Bao, *Sci. Adv.* **2017**, *3*, e1602076.
- [46] A. Håkansson, S. Han, S. Wang, J. Lu, S. Braun, M. Fahlman, M. Berggren, X. Crispin, S. Fabiano, *J. Polym. Sci. Part B Polym. Phys.* **2017**, *55*, 814.
- [47] J. Rivnay, P. Leleux, M. Ferro, M. Sessolo, A. Williamson, D. a. Koutsouras, D. Khodagholy, M. Ramuz, X. Strakosas, R. M. Owens, C. Benar, J.-M. Badier, C. Bernard, G. G. Malliaras, *Sci. Adv.* **2015**, *1*, e1400251.
- [48] S. Wang, J. Xu, W. Wang, G.-J. N. Wang, R. Rastak, F. Molina-Lopez, J. W. Chung, S. Niu, V. R. Feig, J. Lopez, T. Lei, S.-K. Kwon, Y. Kim, A. M. Foudeh, A. Ehrlich, A. Gasperini, Y. Yun, B. Murmann, J. B.-H. Tok, Z. Bao, *Nature* **2018**, *555*, 83.
- [49] C. Lu, W. Y. Lee, C. C. Shih, M. Y. Wen, W. C. Chen, *ACS Appl. Mater. Interfaces* **2017**, *9*, 25522.
- [50] N. Liu, A. Chortos, T. Lei, L. Jin, T. R. Kim, W. Bae, C. Zhu, S. Wang, R. Pfattner, X. Chen, R. Sinclair, Z. Bao, *Sci. Adv.* **2017**, *3*, e1700159.
- [51] F. Xu, M.-Y. Wu, N. S. Safron, S. S. Roy, R. M. Jacobberger, D. J. Bindl, J.-H. Seo, T.-H. Chang, Z. Ma, M. S. Arnold, *Nano Lett.* **2014**, *14*, 682.
- [52] J. Pu, Y. Zhang, Y. Wada, J. Tse-Wei Wang, L.-J. Li, Y. Iwasa, T. Takenobu, *Appl. Phys. Lett.* **2013**, *103*, 023505.
- [53] S.-K. Lee, B. J. Kim, H. Jang, S. C. Yoon, C. Lee, B. H. Hong, J. a Rogers, J. H. Cho, J.-H. Ahn, *Nano Lett.* **2011**, *11*, 4642.
- [54] C. J. Wan, Y. H. Liu, P. Feng, W. Wang, L. Q. Zhu, Z. P. Liu, Y. Shi, Q. Wan, *Adv. Mater.* **2016**, 5878.
- [55] C. J. Wan, Y. H. Liu, L. Q. Zhu, P. Feng, Y. Shi, Q. Wan, *ACS Appl. Mater. Interfaces*

2016, 8, 9762.

- [56] P. P. Atluri, W. G. Regehr, *J. Neurosci.* **1996**, 16, 5661.
- [57] L. Q. Zhu, C. J. Wan, L. Q. Guo, Y. Shi, Q. Wan, *Nat. Commun.* **2014**, 5, 1.
- [58] C. J. Wan, L. Q. Zhu, Y. H. Liu, P. Feng, Z. P. Liu, H. L. Cao, P. Xiao, Y. Shi, Q. Wan, *Adv. Mater.* **2016**, 28, 3557.
- [59] Y. Zang, H. Shen, D. Huang, C.-A. Di, D. Zhu, *Adv. Mater.* **2017**, 29, 1606088.
- [60] C. Wan, G. Chen, Y. Fu, M. Wang, N. Matsuhisa, S. Pan, L. Pan, H. Yang, Q. Wan, L. Zhu, X. Chen, *Adv. Mater.* **2018**, 1801291, 1801291.
- [61] Z. Yu, O. Graudejus, C. Tsay, S. P. Lacour, S. Wagner, B. Morrison, *J. Neurotrauma* **2009**, 26, 1135.
- [62] Z. Liu, X. Wang, D. Qi, C. Xu, J. Yu, Y. Liu, Y. Jiang, B. Liedberg, X. Chen, *Adv. Mater.* **2017**, 29, 1603382.
- [63] D.-J. Guo, S.-J. Xiao, H.-B. Liu, J. Chao, B. Xia, J. Wang, J. Pei, Y. Pan, Z.-Z. Gu, X.-Z. You, *Langmuir* **2005**, 21, 10487.
- [64] Y. Yu, D. Sanchez, N. Lu, *J. Mater. Res.* **2015**, 30, 2702.

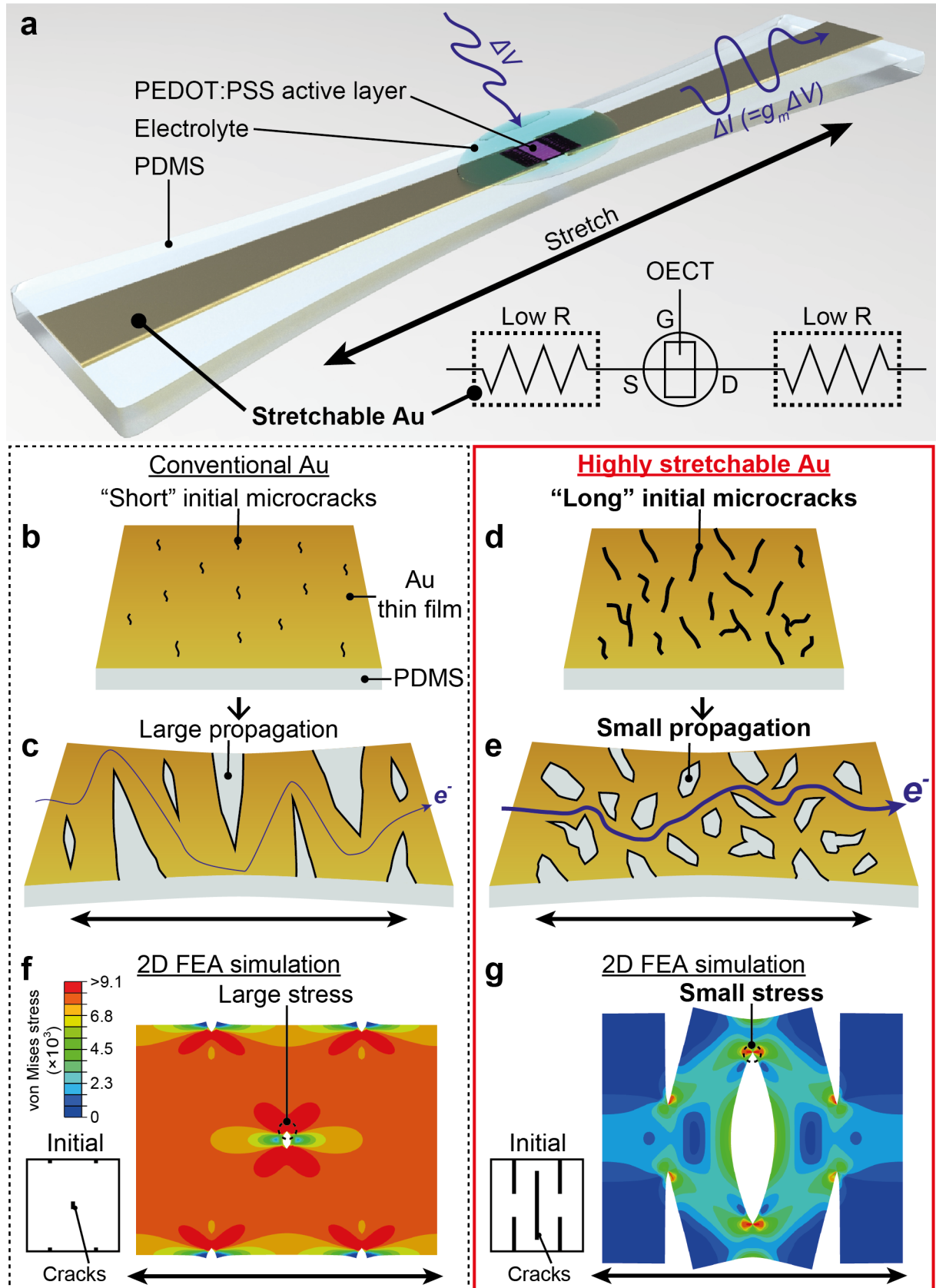


Figure 1. Stretchable OECTs fabricated with highly stretchable microcracked Au. **(a)** A schematic and equivalent circuit of a stretchable OECT upon strain. OECTs amplify the input signals (ΔV) to currents ($\Delta I = g_m \Delta V$), decoupled from the presence of strains due to the high conductance of highly stretchable Au. Schematics of a previously reported stretchable microcracked Au **(b)** without and **(c)** with strain. Schematics of the highly stretchable

microcrack Au (**d**) without and (**e**) with strain. Our highly stretchable Au possesses long initial microcracks, which results in small microcrack propagation and high conductance. (**f,g**) 2D FEA simulation of stress distribution in Au films with short, and long initial microcracks, respectively. A strain of 10% was applied.

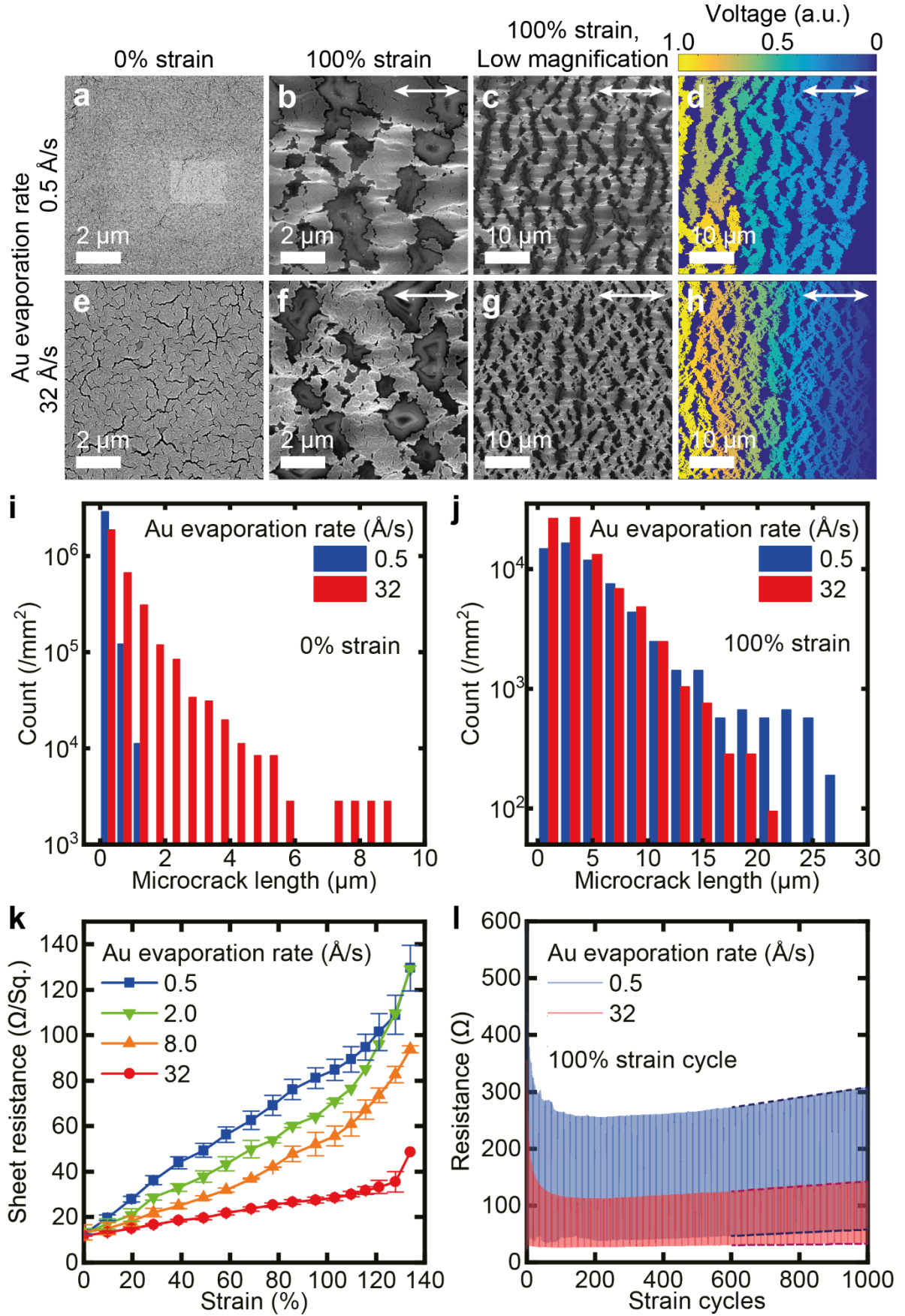


Figure 2. Highly stretchable Au achieved by designing the initial microcracks. (a-c, e-f) SEM images of Au thin films deposited at an evaporation rate of 0.5, and 32 Å/s, respectively. Strain was applied at 0% (a,e) and 100% (b,c,f,g) in lateral direction. (c,g) were taken at

lower magnification than (b,f). Au thin films deposited at 32 Å/s have a large number of long initial microcracks, and the propagation by strain is small. (d,h) Voltage simulation analysis of (c,g), respectively. Virtual voltage was set in the parallel direction with strain. (i,j) Microcrack length histograms of Au thin films with 0, and 100% strain, respectively. Au films were deposited at an evaporation rate of 0.5, and 32 Å/s. This data was obtained from image analysis of SEM images. High evaporation rates resulted in longer initial microcrack formations, yet smaller propagations by strain than slow evaporation rates. (k) Sheet resistance-strain characteristics of Au thin films deposited at different evaporation rates. In accordance with the SEM images and the image analysis (a-h), Au thin films deposited at high evaporation rates showed smaller sheet resistances at high strain.

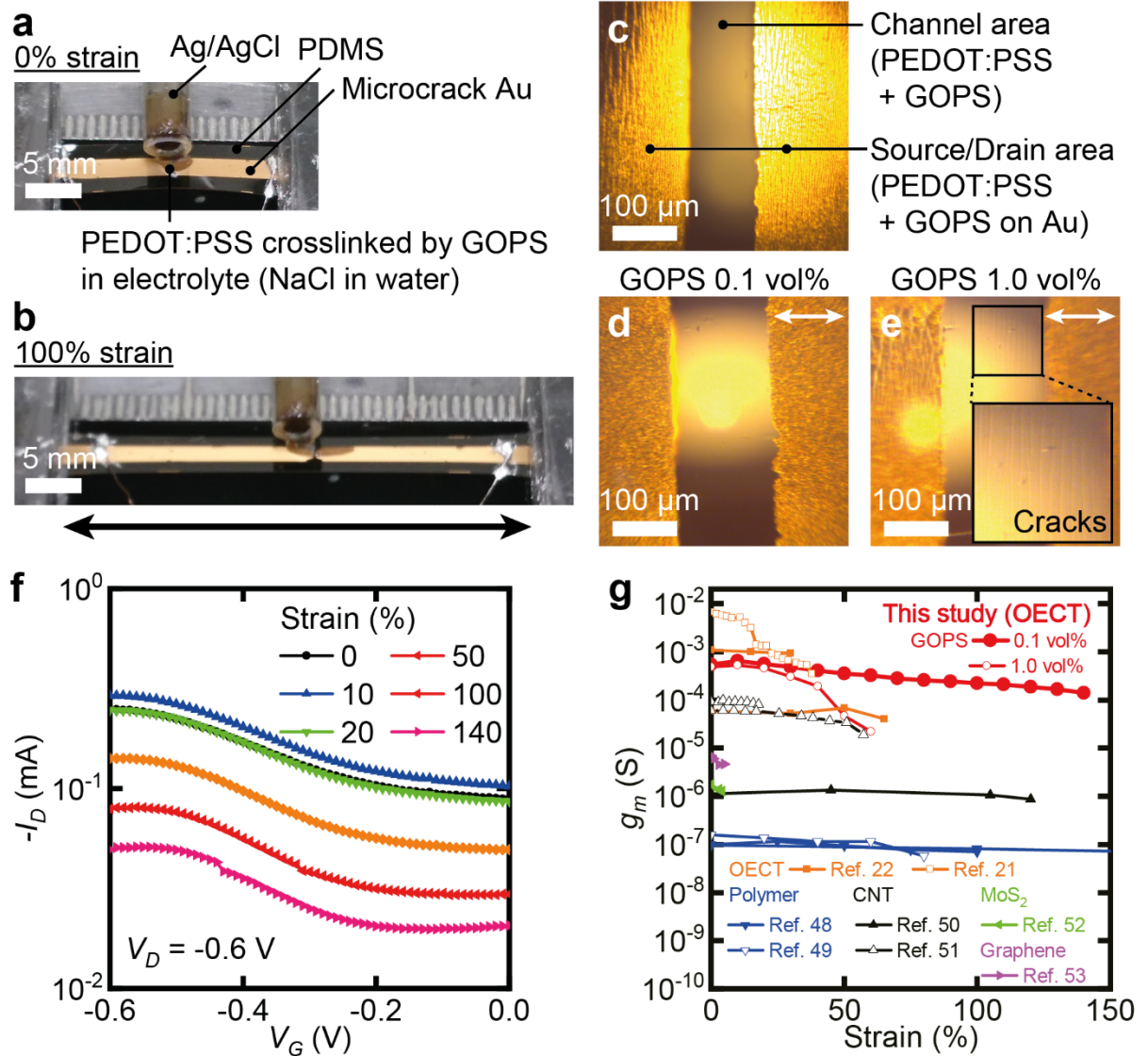


Figure 3. Fully stretchable OEETs. (a,b) Photographs of stretchable OEETs without, and with 100% strain, respectively. (c-e) Optical microscope images of channels in OEETs without strain (c), and with 100% strain (d,e). GOPS concentration in the solution to form active layers was changed to 0.1 vol% (d), and 1.0 vol% (e). (f) Transfer characteristics of OEETs with different strains. (g) Maximum g_m dependence on strain with a comparison with previous reports on intrinsically stretchable transistors.

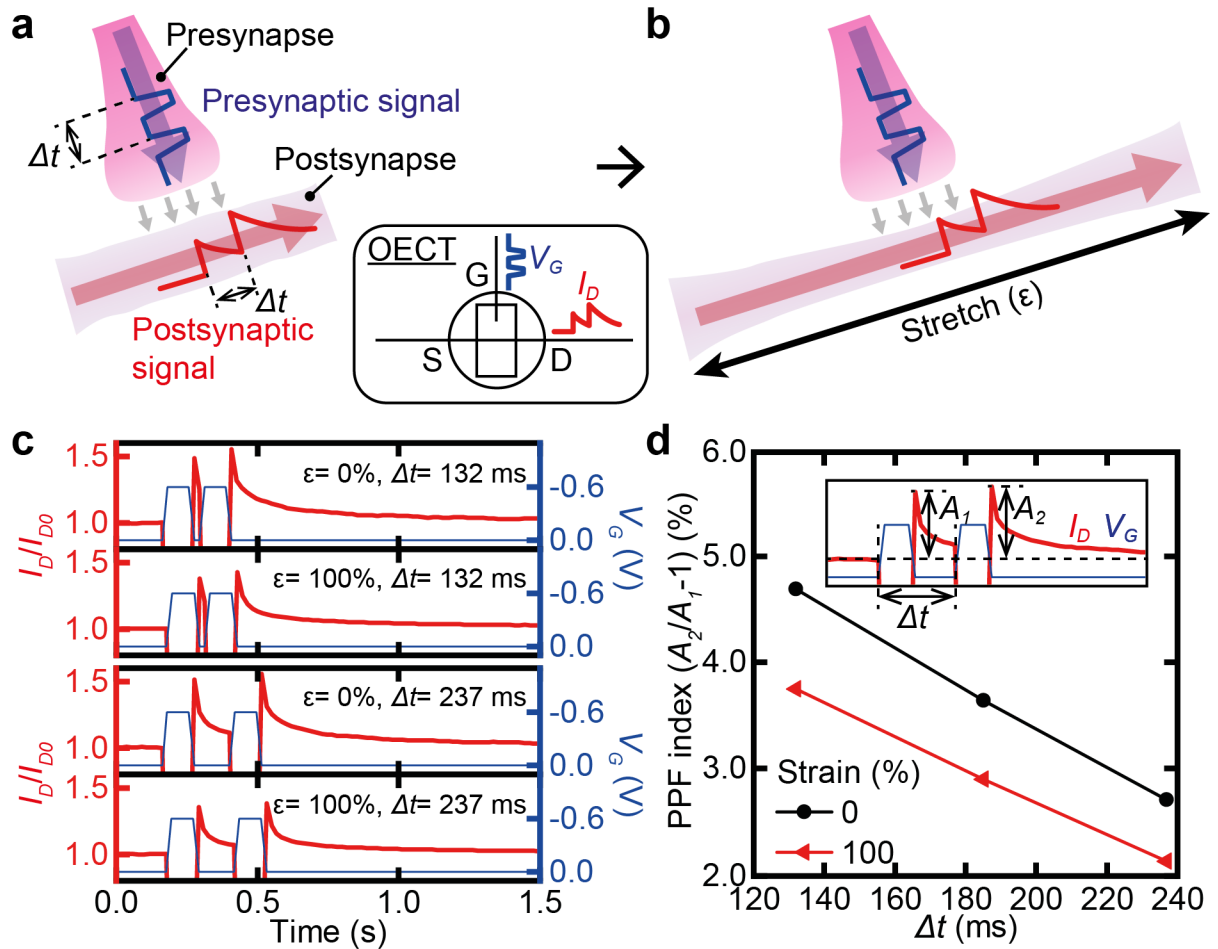


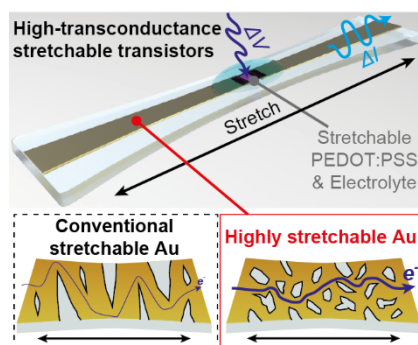
Figure 4. Fully stretchable synaptic transistors. (a,b) Schematics of the electrical signal transfer in synapse without and with strain. The short-term plasticity of signals in synapses was emulated by stretchable OECTs. (c) Normalized excitatory postsynaptic current by paired-pulse facilitation (PPF) of OECTs with 0 and 100% strain. The duration of pulse is fixed to 96 ms. (d) PPF index dependence on the intervals of two spike signals. During the measurement, strains were applied to the OECTs by 0 and 100%.

The highest transconductance in fully stretchable transistors is reported, which contributes to the realization of highly conformable and sensitive wearable sensors. This is enabled by highly stretchable microcrack Au conductors with the lowest sheet resistance at high strain (>50%) among the reported stretchable Au thin film conductors. Furthermore, our transistors showed synaptic transistor characteristics, which is critical for the realization of artificial intelligence in soft robotics.

Keyword Stretchable electronics, Organic electrochemical transistors, Stretchable conductors

N. Matsuhisa, Y. Jiang, Z. Liu, G. Chen, C. Wan, Y. Kim, J. Kang, H. Tran, H.-C. Wu, I. You, Z. Bao*, and X. Chen*

High-transconductance stretchable transistors achieved by controlled gold microcrack morphology



Supporting Information

High-transconductance stretchable transistors achieved by controlled gold microcrack morphology

Naoji Matsuhisa, Ying Jiang, Zhiyuan Liu, Geng Chen, Changjin Wan, Yeongin Kim, Jiheong Kang, Helen Tran, Hung-Chin Wu, Insang You, Zhenan Bao, and Xiaodong Chen**

2D FEA Simulation

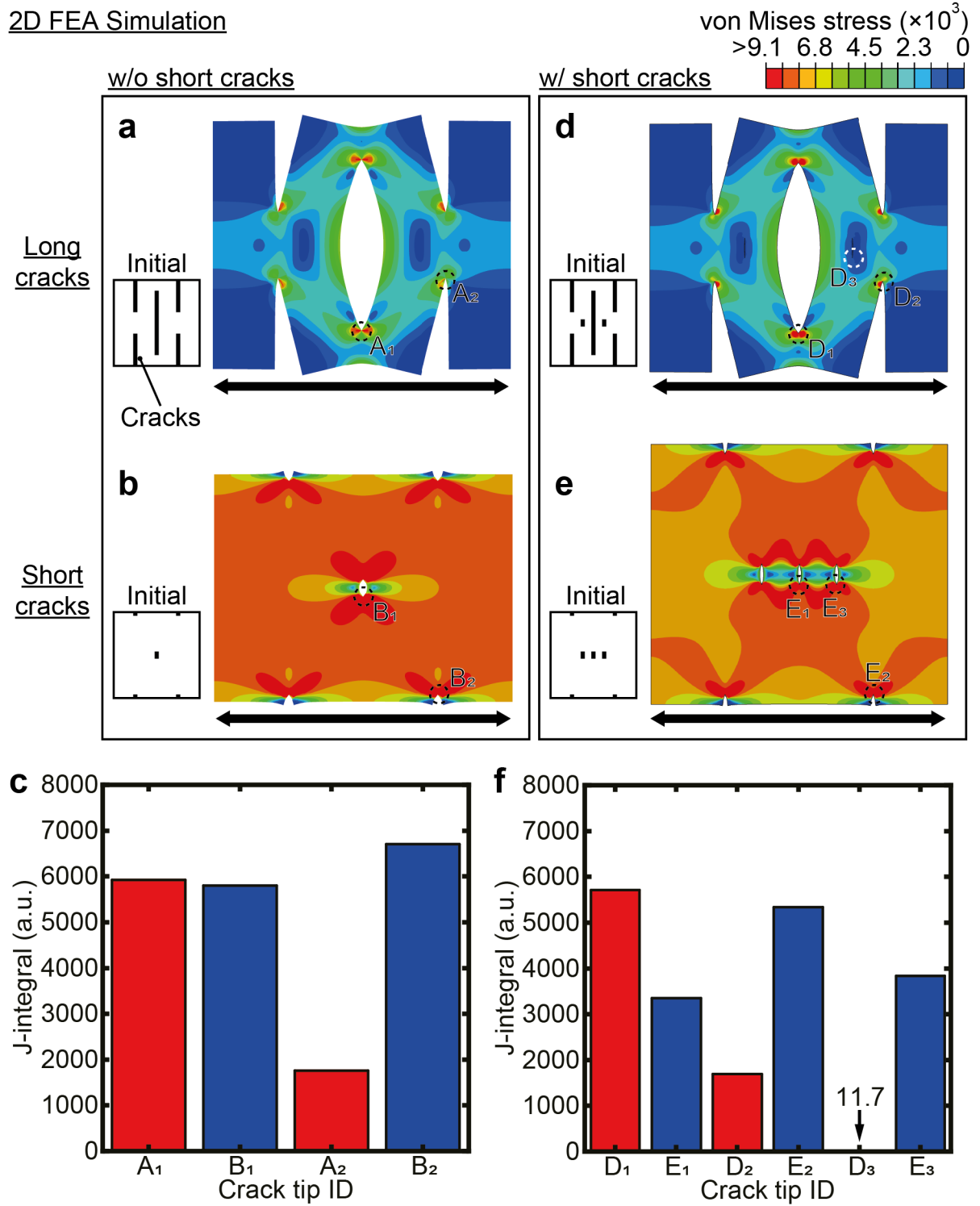


Figure S1. 2D FEA simulations for the analysis of stress and J-integral at tips. (a,b) Initial crack designs and the result of stress mapping with long, and short cracks (Figure 1g,f), respectively. (c) J-integrals in crack tips shown in a,b. The value represents energy dissipated at each fracture. The significantly low value at A₂ explains that smaller degree of strain energy is consumed to open this crack tip than the other crack tips. (d,e) The stress relaxation effect to the surrounding small cracks by the long, and short initial cracks, respectively. (f) J-integrals in crack tips shown in d,e. The stress relaxation by the long cracks is reflected by the low value at D₃.

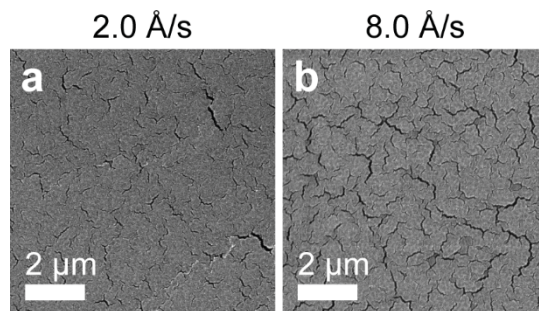


Figure S2. Initial microcracks of Au films deposited on PDMS with different evaporation rate. (a) 2.0 Å/s. (b) 8.0 Å/s.

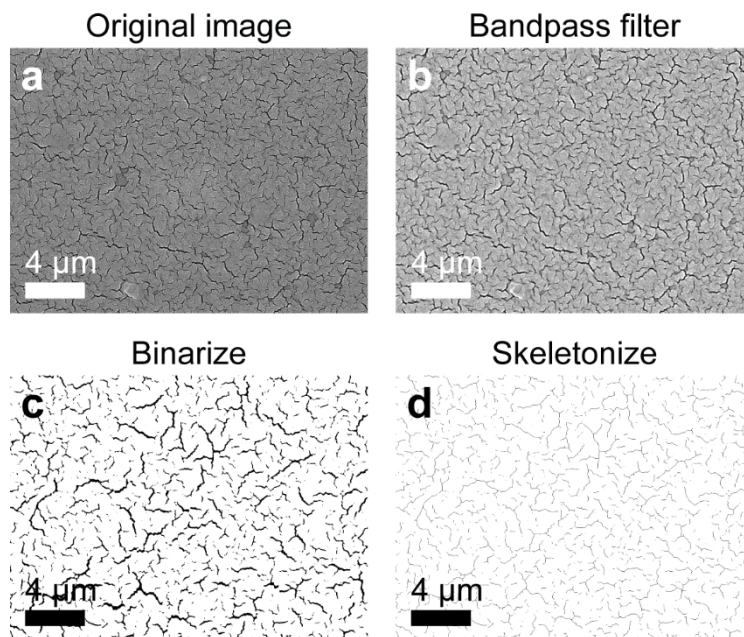


Figure S3. Image analysis for measuring length of microcracks. (a) Original image. (b) Image processed by bandpass filter to make edge of microcracks clear. (c) Binarized image. (d) Skeletonized image. The area of each line matches with the length of microcracks.

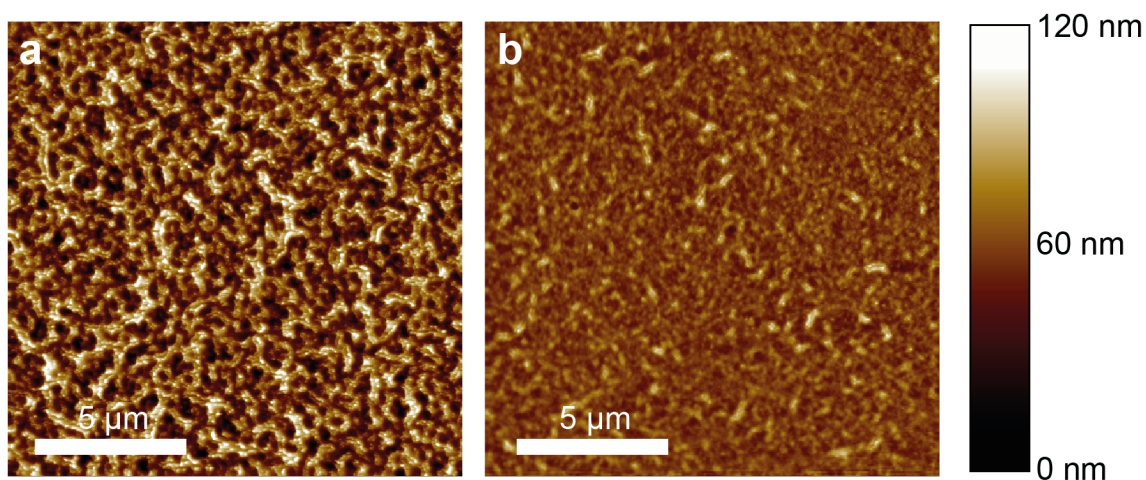


Figure S4. Atomic force microscope (AFM) images of Au thin films deposited at 32 Å/s (a) and 0.5 Å/s (b).

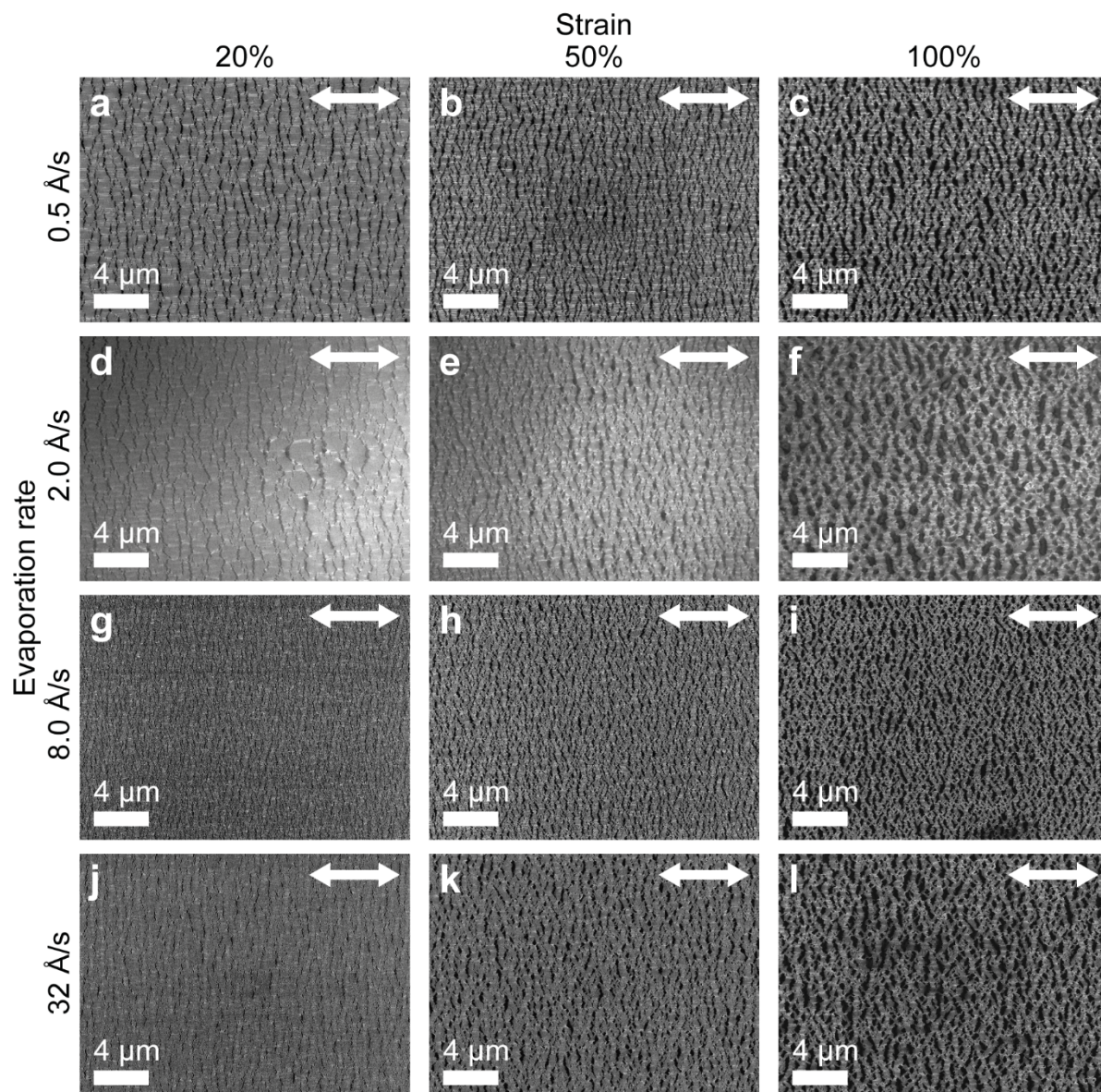


Figure S5. SEM images of Au films evaporated with different rate and strains. Evaporation rate: (a-c) 0.5 Å/s; (d-f) 2.0 Å/s; (g-i) 8.0 Å/s; (j-l) 32 Å/s. Strain: (a,d,g,j) 20%; (b,e,h,k) 50%; (c,f,i,l) 100%.

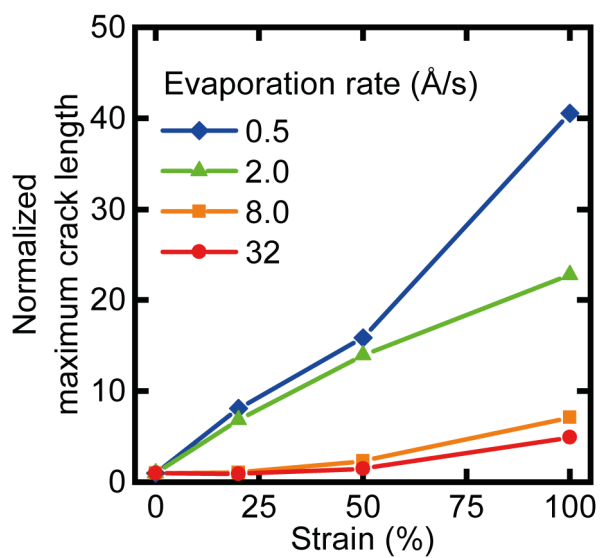


Figure S6. Microcrack propagations obtained from SEM images. Normalized maximum microcrack length was obtained by dividing maximum microcrack length at each strain by maximum microcrack length at 0% strain. Au films deposited at high evaporation rate showed small microcrack propagations. For 0% strain, SEM images with magnification of $\times 5k$ were used, and, for the other strains, those of $\times 2k$ were used because of the nominal microcrack size difference.

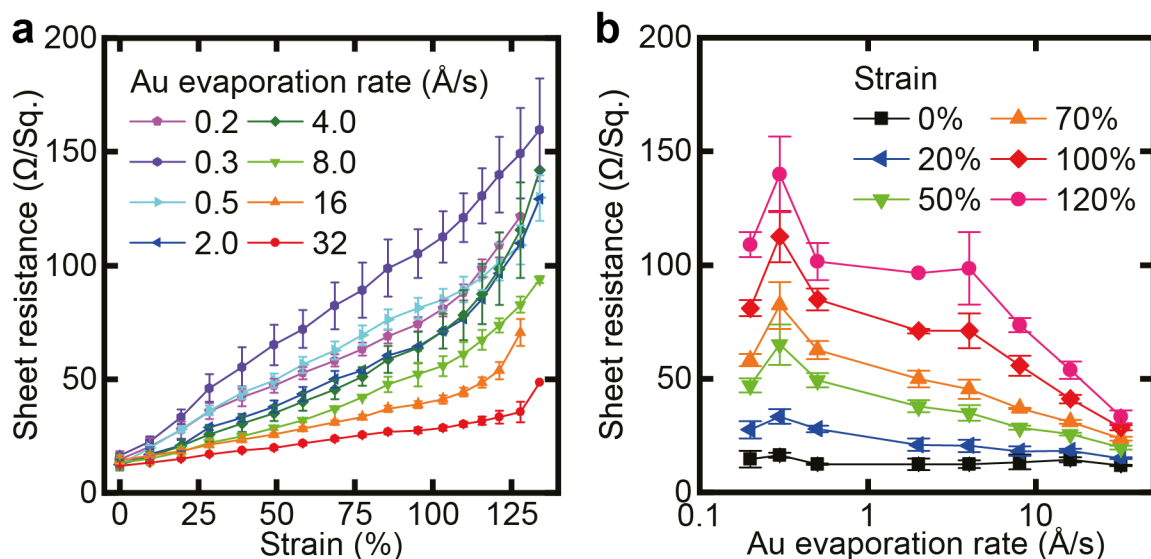


Figure S7. Detailed investigations in the effect of Au evaporation rate in sheet resistance at strains. **(a)** Sheet resistance-strain characteristics with different Au evaporation rates. **(b)** Sheet resistance-Au evaporation rate characteristics with different strains. Data for 0.5, 2.0, 8.0, and 32 $\text{\AA}/\text{s}$ are identical with those in Figure 2k.

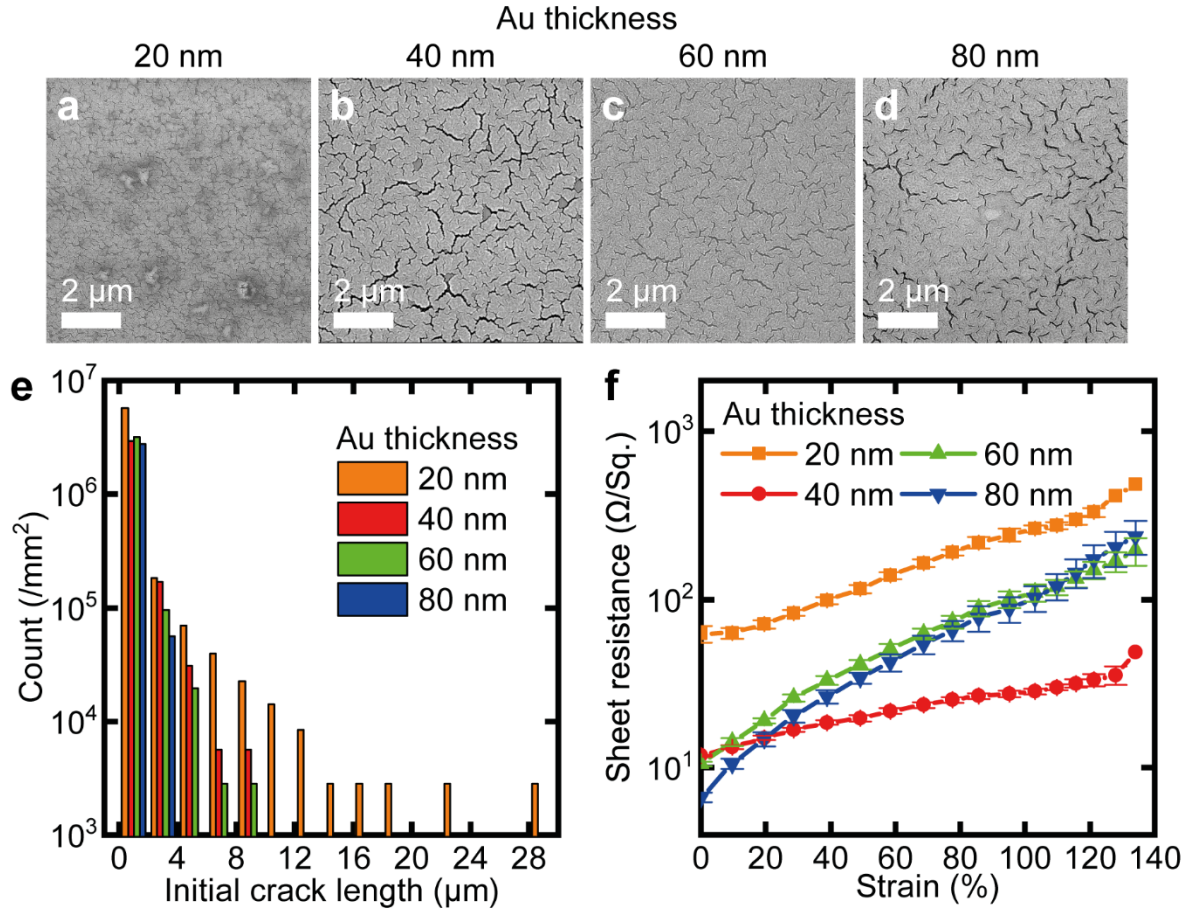


Figure S8. Au thickness dependence in initial microcrack formation and conductance at strains. (a,b,c,d) SEM images of Au thin films with thickness of 20, 40, 60, and 80 nm, respectively. (e) Initial microcrack length and the count obtained from the image analysis of SEM images. The total number of microcracks in 20 nm thick Au thin films was twice as large as the other Au thin films. (f) Sheet resistance-strain characteristics of Au thin films with thickness of 20, 40, 60, and 80 nm. Data for 40 nm are identical with those in Figure 2k. All the Au was deposited at evaporation rate of 32 $\text{\AA}/\text{s}$.

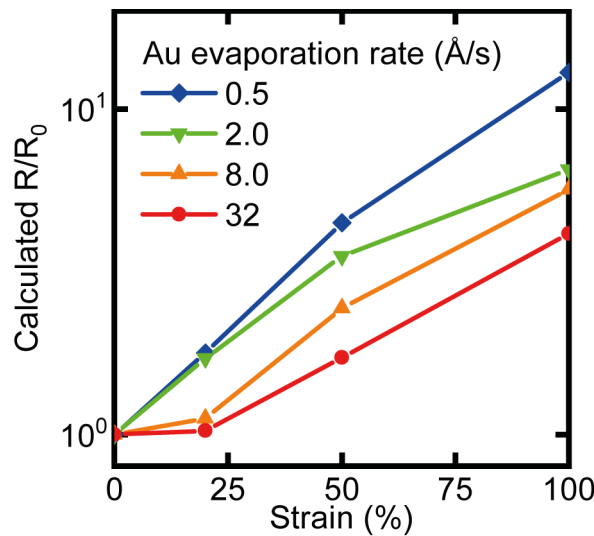


Figure S9. Resistance change (R/R_0) calculated from voltage simulation analysis of SEM images. For 0% strain, SEM images with magnification of $\times 5\text{k}$ were used, and, for the other strains, those of $\times 2\text{k}$ were used because of the nominal microcrack size difference.

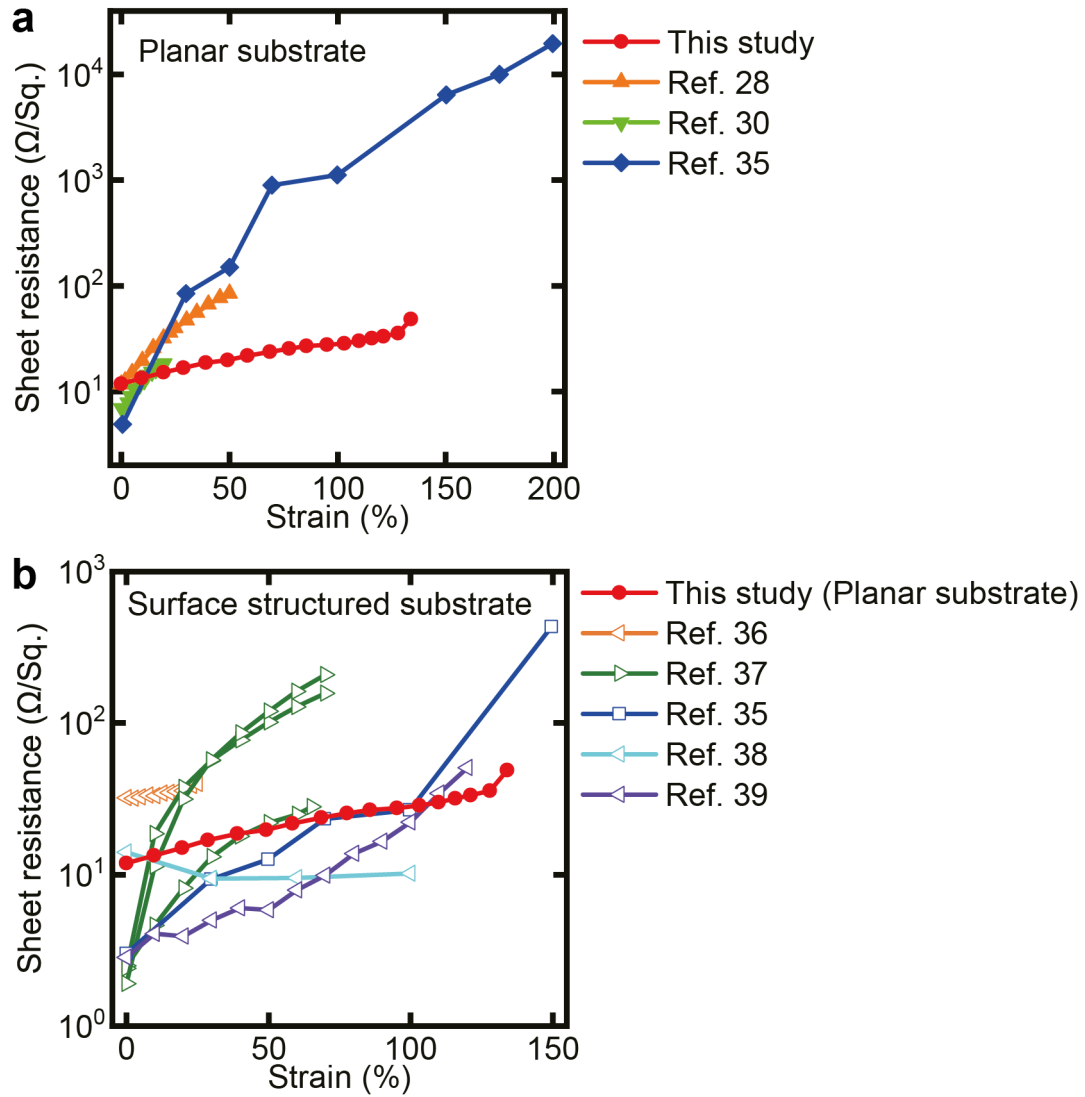


Figure S10. Comparison with previous studies about stretchable Au thin films on elastomer substrates. **(a)** Comparison with Au thin films on planar substrate. **(b)** Comparison with Au thin films on surface structured substrates.

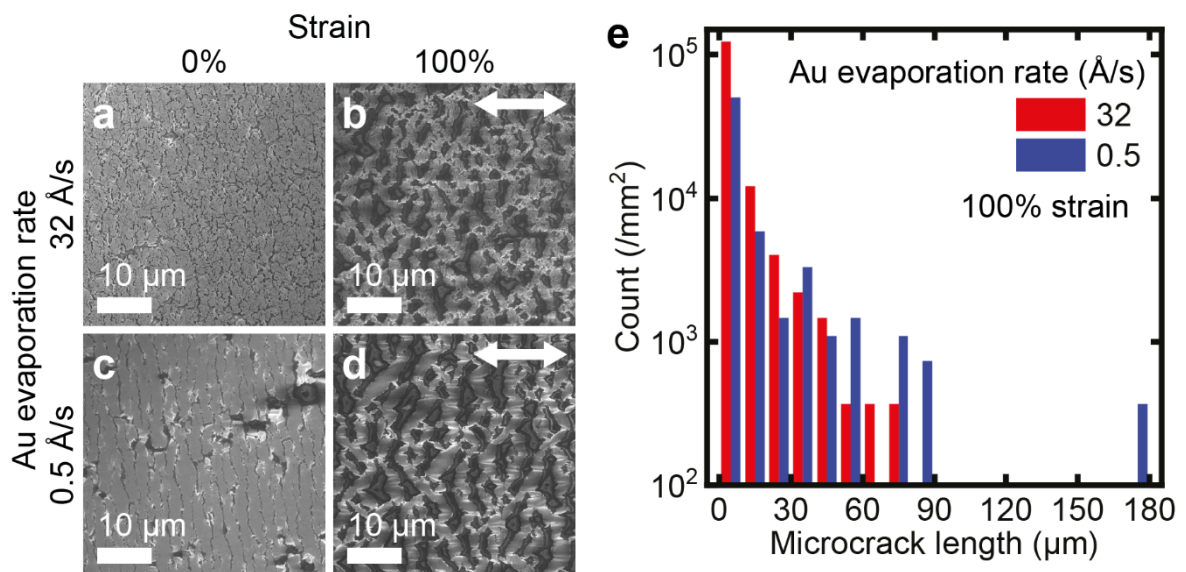


Figure S11. SEM images of Au after 1000 cycles of 100% strain. Au was evaporated at 32 Å/s (a,b), and 0.5 Å/s (c,d). SEM images were taken with 0% strain (a,c), and 100% strain (b,d). (e) Microcrack length histograms in b,d. High evaporation rates resulted in smaller microcrack propagations.

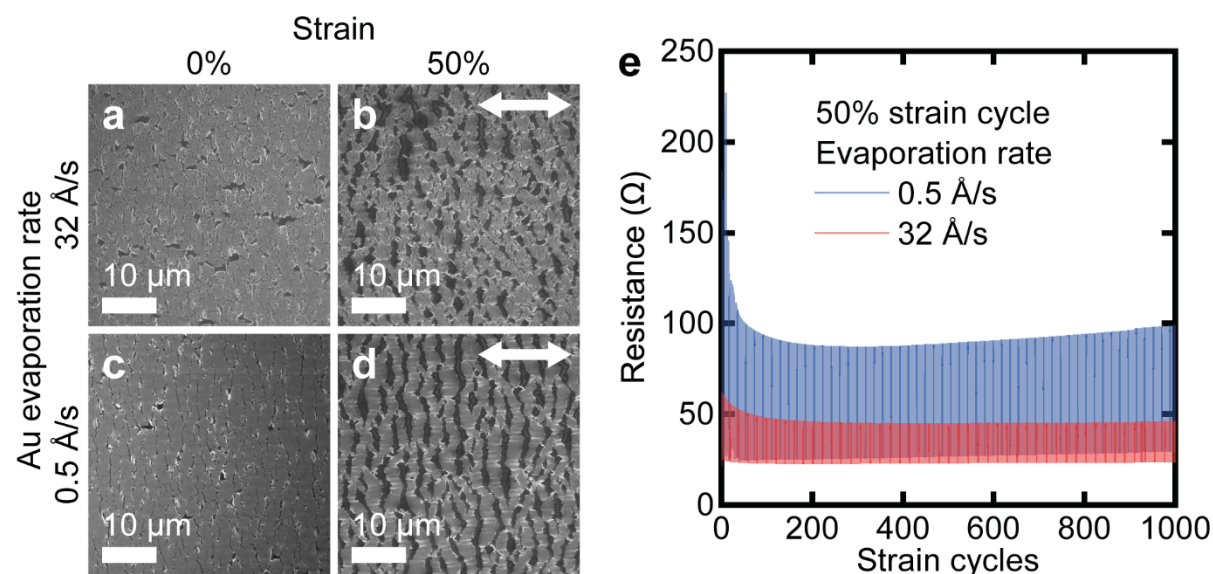


Figure S12. High cyclic strain durability of highly stretchable Au against 1,000 cycles of 50% strains. (a-d) SEM images of Au after 1000 cycles of 50% strain. Au was evaporated at 32 Å/s (a,b), and 0.5 Å/s (c,d). SEM images were taken with 0% strain (a,c), and 50% strain (b,d). Au films deposited at 32 Å/s still showed small microcrack propagations although those at 0.5 Å/s showed vertically propagated large microcracks. (e) Resistance of Au films deposited at 0.5 and 32 Å/s during cyclic strains (50%). Au films deposited at 32 Å/s still showed reduced sheet resistance both in stretched (50% strain) and relaxed (0% strain) states. Films were prepared in width, and length of 1, and 2 cm, respectively.

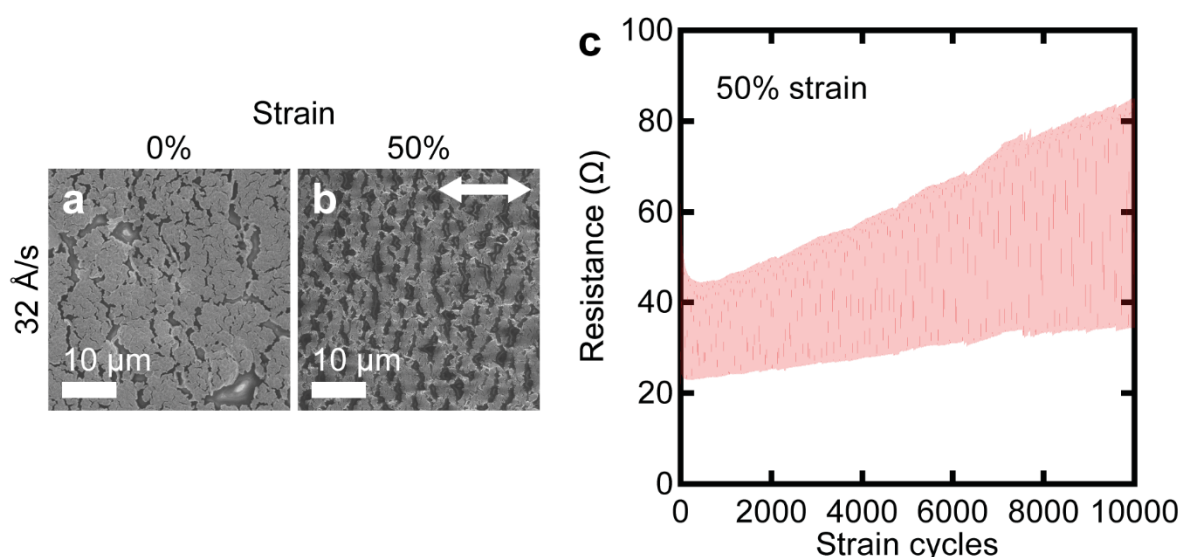


Figure S13. High cyclic strain durability of highly stretchable Au against 10,000 cycles of 50% strains. (a,b) SEM images of Au after 1000 cycles of 50% strain. Au was evaporated at 32 Å/s. SEM images were taken with (a) 0% strain, and (b) 50% strain. (c) Resistance of highly stretchable Au during cyclic strains (50%). Films were prepared in width, and length of 1, and 2 cm, respectively.

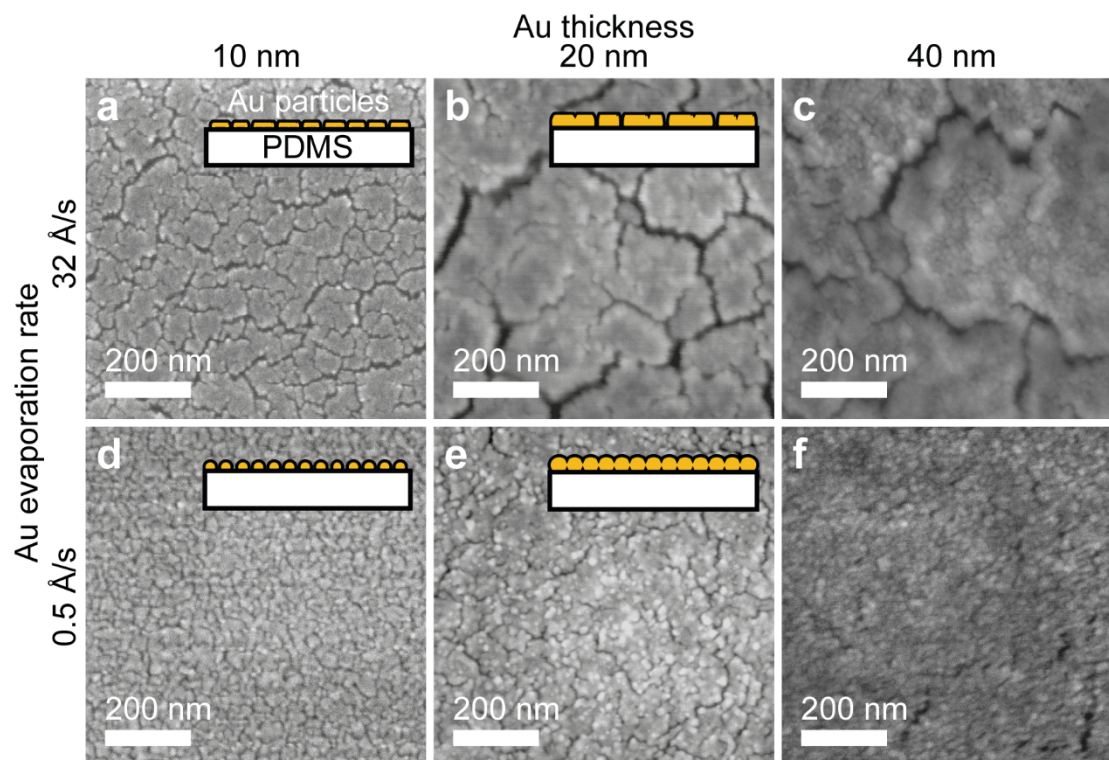


Figure S14. SEM images to describe Au thin film growth with different evaporation rates (**a,b,c**: 32 Å/s, **d,e,f**: 0.5 Å/s, **a,d**: 10 nm, **b,e**: 20 nm, **c,f**: 40 nm). Au films deposited at fast evaporation rate (32 Å/s) showed large connected Au particles, although those at slow evaporation rate (0.5 Å/s) showed uniformly distributed small particles. Films deposited 10 nm of Au were not conductive. Increasing thickness of Au resulted in shorter microcracks because Au deposition can fill the gaps in microcracks.

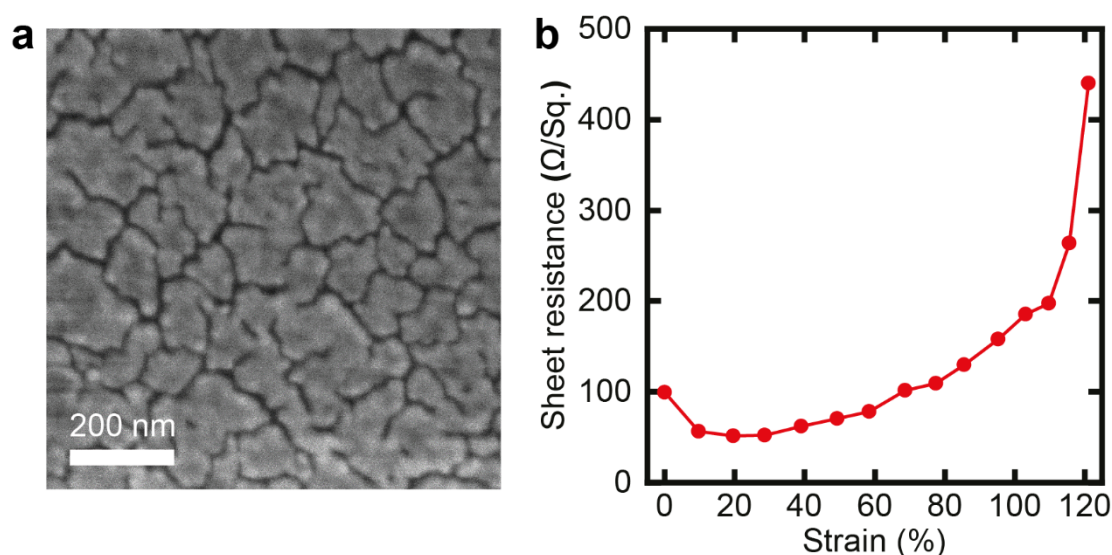


Figure S15. Stretchable microcracked Ag thin film conductors. Ag thin film with a thickness of 40 nm was deposited at 32 Å/s with a 3 nm Cr adhesion layer on a PDMS substrate. **(a)** SEM image. **(b)** Sheet resistance-strain characteristic.

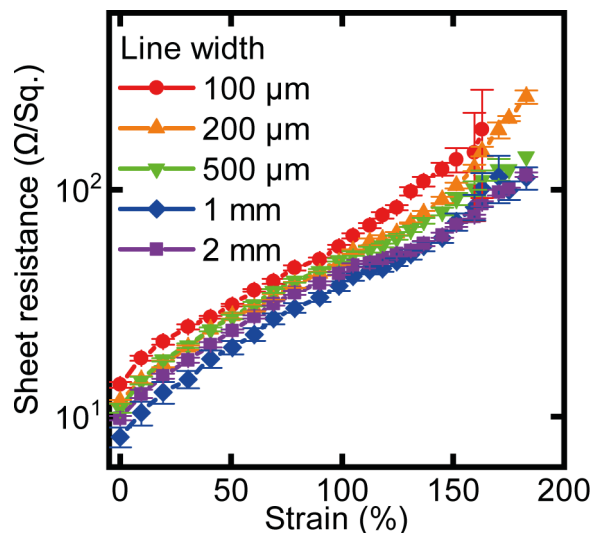


Figure S16. Miniaturization of highly stretchable Au. Line width was changed from 100 μm to 2 mm while the length was set to 2 cm.

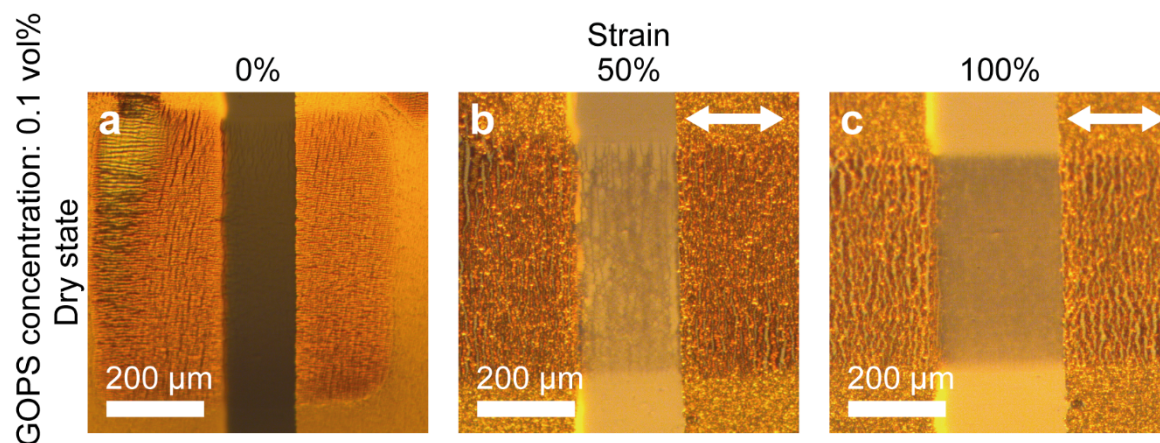


Figure S17. Optical microscope images of PEDOT:PSS film in dry environment with strains of (a) 0%, (b) 50%, and (c) 100%, clearly describing the small stretchability.

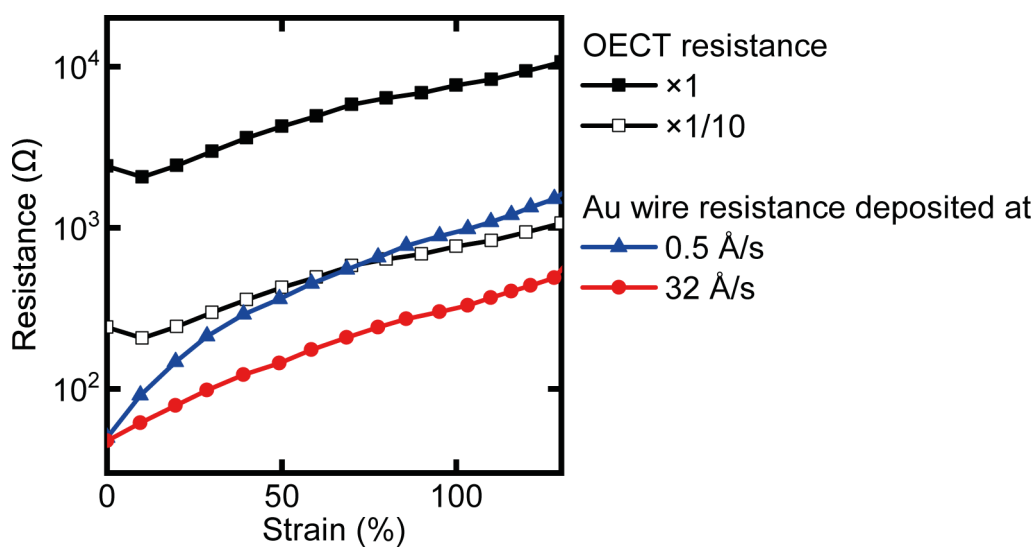


Figure S18. Resistance comparison between whole OECT and Au wire deposited at 0.5 and 32 $\text{\AA}/\text{s}$. Au wire deposited at 32 $\text{\AA}/\text{s}$ showed resistance lower than one tenth of whole OECT.

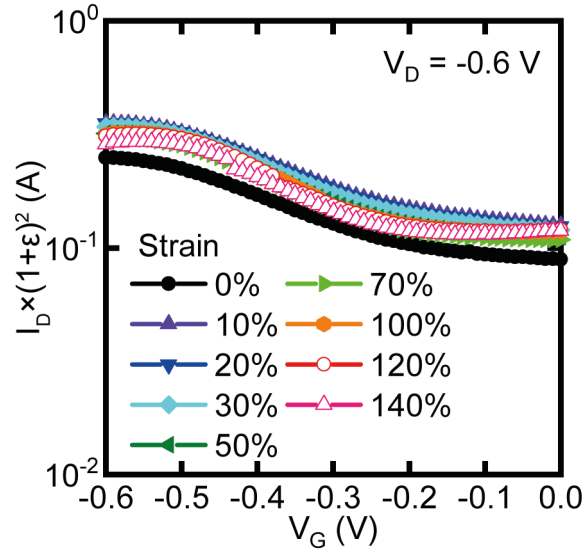


Figure S19. Transfer characteristics of intrinsically stretchable OECTs with different strain. Here, the drain current (I_D) was normalized by the geometrical change with an assumption that total volume of PEDOT:PSS does not change by strain. Applied strain is denoted by ϵ .

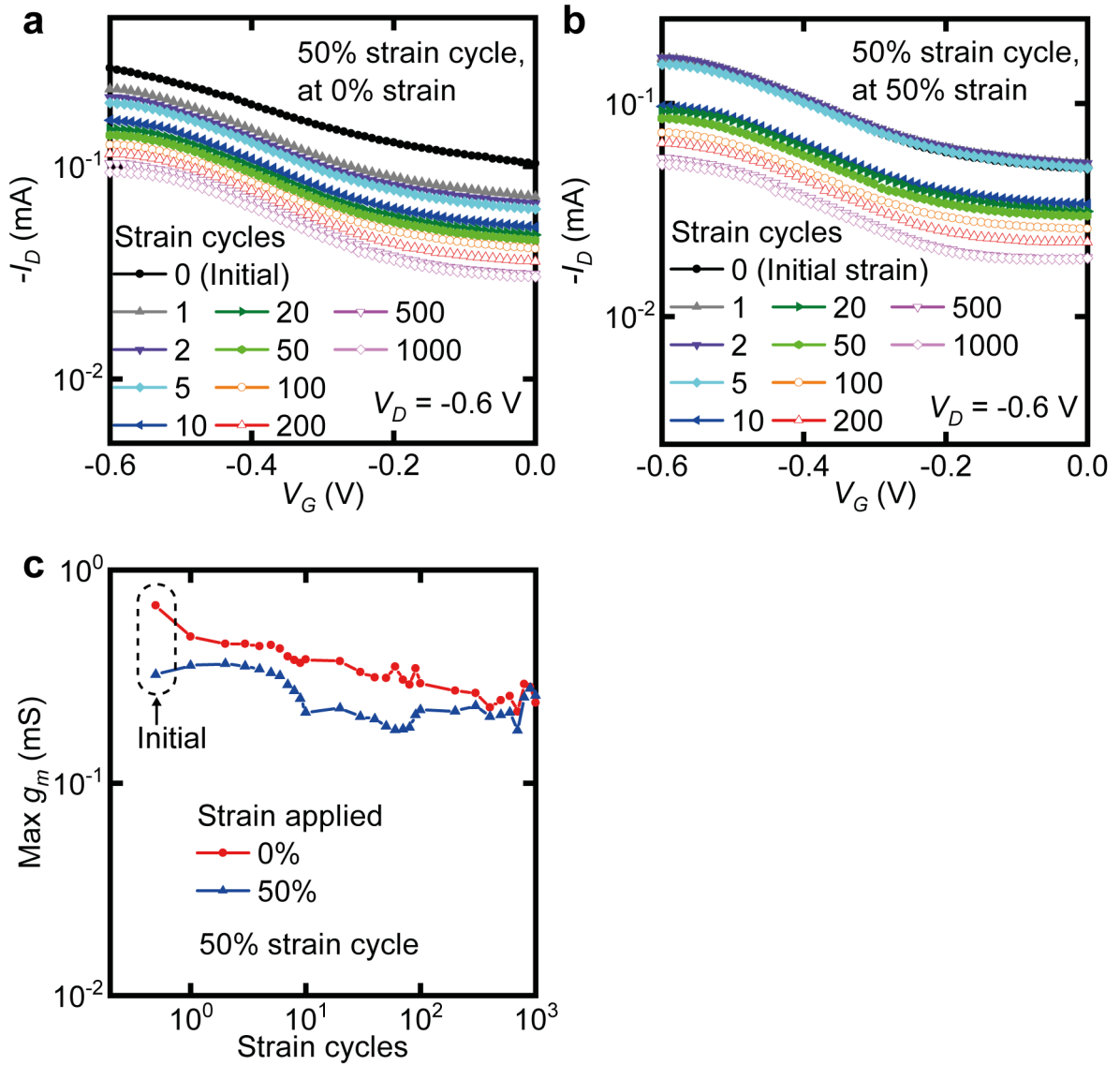


Figure S20. Cyclic durability of intrinsically stretchable OECTs against 1,000 cycles of 50% strain. (a,b) Transfer characteristics of OECT in relaxed state (0%), and stretched state (50%), respectively. (c) Maximum g_m dependence on the strain cycles.

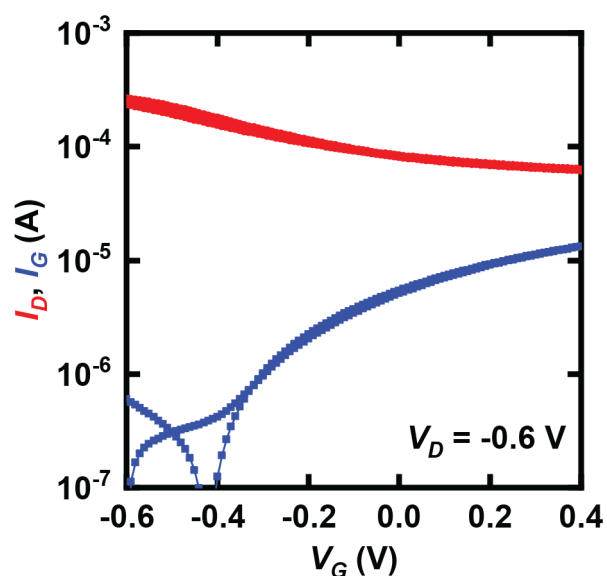


Figure S21. Transfer characteristics of stretchable OECTs with active materials made from 1 vol% GOPS concentration.